Benjamin Lang, BSc.

Considerations on orifice plate flow measurement of heavily pulsating flow

MASTER'S THESIS

to achieve the university degree of

Diplom-Ingenieur

Master's degree programme: Technical Physics

submitted to

Graz University of Technology

Supervisor

Univ.-Prof. Dipl.-Phys. Dr.rer.nat. Wolfgang von der Linden

Institute of Theoretical and Computational Physics

Graz, June 2015

AFFIDAVIT

I declare that I have authored this thesis independently, that I have not used other than the declared sources/resources, and that I have explicitly indicated all material which has been quoted either literally or by content from the sources used. The text document uploaded to TUGRAZonline is identical to the present master‘s thesis dissertation.

Date

Signature

Acknowledgments

I would like to use this space to express my sincere thanks to my supervisor at the Graz University of Technology, Univ.-Prof. von der Linden for his expertise and assistance in the realization of this thesis and for enabling the cooperation with AVL List.

I am particularly grateful to Dr. Harms from AVL List for his guidance and the knowledge shared in the numerous consultations during the course of this work. From the AVL department MM, I would like to express my thanks Dr. Kudlaty and Dr. Wiesinger for the opportunity of this thesis and the whole department for advice and technical assistance. In addition, I would like to thank Dr. Bergmann and his department at AVL List for their support in subject-specific, technical and legal matters and for providing the necessary equipment and facilities for this thesis.

Abstract

This thesis covers a study on the applicability of using a one-dimensional, unsteady momentum equation at an orifice differential pressure flow meter for time resolved mass flow measurement of intake air and exhaust gas of internal combustion engines.

A theoretical investigation on unsteady flow behavior in highly pulsating flows indicates, that conventional unsteady inertia theory in the form $\Delta p = \frac{A}{\rho} J^2 + B \frac{\partial J}{\partial t}$ [1] with a constant steady coefficient A and constant inertance B, is only capable of correctly modeling pulsation induced flow effects to a certain extent. When pulsation frequencies are high and amplitudes are large compared to mean flow velocity, unsteady effects will increase measurement uncertainties.
Computational fluid dynamics (CFD) simulations for both steady and pulsating flows were applied to an orifice meter in corner tapping configuration to study the flow behavior and errors of conventional mass flow equations and an alternative mass flow equation that incorporates unsteady, dissipative effects and fast density changes. The steady flow simulations revealed the importance of flow stagnation, i.e. radial pressure and flow distribution effects, at an orifice flow meter with the pressure tappings placed close to the orifice plate. Only a fraction of the measured pressure difference in such a configuration can be attributed to the Bernoulli effect. In the CFD simulations for pulsating flows, deviations in radial pressure- and flow-distribution from the steady distributions, which underlie unsteady mass flow calculations, were identified to be the cause of high uncertainties. For heavily oscillating flows (e.g. 300 Hz with mean flow), minimum relative mass flow errors of 10 % were encountered. Noteworthy increases of measurement errors up to

20 %, were introduced by inertance values as recommended in ISO/TR 3313 [2]. Mass flow calculations on the simulated inlet flow of a two stroke engine running at 4000 *rpm*, yielded relative mass flow errors around 1 % and root mean square (RMS) errors below 2 %, supporting the basic applicability of the method. Deviations in the pulsation cycle only occurred when local flow reversals were present at the location of measurement, i.e. when the pulsation amplitude is in the order of the mean mass flow. However, significant increases in mass flow and RMS errors became apparent for over- and underestimated inertance coefficients, which produced square-root- and inertial-errors, respectively.

A resonance tube, acoustically driven by a loudspeaker, with the possibility for superimposed mean flow, was set up for an experimental determination of the calibration parameters of a specific orifice meter. Steady calibration measurements were in good agreement with simulation values, but revealed considerable oscillations in the measured pressure signals. During resonance mode measurements, these oscillations could be identified as resonances inside the pressure measurement system of the orifice meter, possibly stemming from a Helmholtz resonator behavior of the connected gauge lines and volumes.
Impedance calculations for the standing waves in the main resonance pipe at resonance excitation, allowed an assessment of the pulsation amplitude at 30 Hz for reference purposes and demonstrated conformity with the unsteady mass flow calculations. At higher frequencies, the resonances in the pressure measurement system and the associated high uncertainties prohibited an exact determination of the calibration parameters. An adaptation of the orifice meter, i.e. eliminating the resonance behavior of the device itself, could allow for a more precise determination of the calibration parameters in future measurements.

In addition, a method for fast and accurate temperature and density determination is introduced, combining two thermocouple compensation techniques for temperature measurement with an adiabatic correction for pressure pulsation induced temperature changes.

Contents

List of Figures

1. Introduction

The steady drop of exhaust emission limits for internal combustion engines of automobiles is continuously driving the need for an improvement of accuracy in measurement of flow rates, since measurements of pollutant concentrations commonly rely on flow rates for reference. An additional requirement for precise air to fuel ratios to further optimize the combustion process, altogether propels a demand for highly accurate, time resolving measurements for both intake air and exhaust gas, that assist in realizing the technically achievable reductions.

Differential pressure flow meters have been employed in intake and exhaust gas flow measurement for quite some time, due to their simple structure, which makes them less susceptible to the harsh conditions in an exhaust environment compared to devices relying on more complex or contamination prone sensing elements. The absence of fast response pressure transducers to precisely resolve pulsations in the intake or exhaust lines and shortcomings in the mathematical description of pulsating flow, so far resulted in the need for supplemental flow stabilizing and calming modules which in turn impacted the combustion unit under measurement.

AVL List GmbH already conducted a feasibility study on the use of an orifice meter in pulsating exhaust flow environments, which concluded that orifice meters are capable of accurately delivering a time resolved mass flow measurement under some conditions. High error rates and inconsistencies in measurement performance in a variety of cases in laboratory experiments and in the exhaust of an engine, however, inhibited a clear identification of the applicability of this type of measurement and led to further questions about the underlying mathematical model.

This work in cooperation of the University of Technology Graz and AVL List GmbH, aimed to further investigate and extend the scope of applicability for a time resolved flow measurement in highly pulsating intake and exhaust gas with the use of an orifice flow meter. Theoretical considerations about the flow at orifices in a pulsating environment have been followed by an experimental study, investigating a possible test and calibration setup for orifice meters.

2. Theoretical Background and Fundamentals of Orifice Flow

2.1. Intake Air and Exhaust Gas Flow

Flow measurement of intake air and exhaust gases of internal combustion engines has to deal with various harsh circumstances, that are not present in other measurement environments. The different stages in the combustion process and the associated rapid opening and closing of the cylinder valves of an engine to take air/fuel into and emit the exhaust gas out of the cylinders, creates pressure waves, that travel down the intake and exhaust lines. Pressure differences of several atmospheres between cylinders and exhaust system are being compensated and result in significant density changes of the gases [3]. The pressure waves subsequently cause a continuous acceleration and deceleration of the air or gas inside the ducts and as a consequence, lead to a mean flow to and from the engine with pulsations superimposed, which can locally reverse the direction of flow. The periodicity of the pulsations is depending on the rotational speed of the engine U $[rpm]$, the amount of cylinders/pistons C that are operated at the same time and the number of strokes N a piston has to complete for one cycle. An assessment of the main frequency f that will be present in the connected lines, can be made by the simple formula given by [4]:

$$f = \frac{2}{N}\frac{U \cdot C}{60} \quad . \tag{2.1}$$

For a typical four stroke engine with four cylinders and rotational speeds up to 7500 rpm [5], this implies pulsation frequencies up to 250 Hz that have to be dealt with in intake and exhaust lines. However, as number of strokes, cylinders and rotational speeds are increased, the extent of the pulsation effects are somewhat attenuated.
Fast temperature transitions between about 300 $°C$ at idle conditions and up to 800 $°C$ at maximum power in exhaust lines [3, 5] are the cause of additional changes in gas properties and density, that have to be considered in the flow measurement process.

2.2. Fluid Mechanics

Before discussing the specific details of the flow of intake air and exhaust gases through orifice meters, it is useful to review some fundamentals of fluid mechanics. Two *basic laws* in continuum mechanics, the continuity equation and the momentum equation are shortly discussed, since those will be later applied to the problem at hand.

2.2.1. Continuity Equation

For any arbitrarily defined control region (CR) in a fluid, which may be moving and deforming, the basic law of conservation of mass has to hold. In sum, the time rate of change of mass in the CR has to equal the mass flow into and out of the control region. As formulated in [6, 7], this is given by:

$$\frac{\mathrm{d}}{\mathrm{d}t} m_{V(t)} + \oint\limits_{\partial V(t)} \rho(\vec{x},t)\big(\vec{v}(\vec{x},t) - \vec{w}(\vec{x},t)\big) \cdot \, \mathrm{d}\vec{S} =$$

$$\frac{\mathrm{d}}{\mathrm{dt}} \int\limits_{V(t)} \rho(\vec{x},t) \; \mathrm{d}V + \oint\limits_{\partial V(t)} \rho(\vec{x},t)\big[\big(\vec{v}(\vec{x},t) - \vec{w}(\vec{x},t)\big) \cdot \vec{n}(\vec{x},t)\big] \; \mathrm{d}S = 0 \quad . \tag{2.2}$$

Where $V(\vec{x},t)$ is an arbitrary volume moving with velocity $\vec{w}(\vec{x},t)$, $\vec{S}(\vec{x},t)$ is its surface vector, normal to the surface and pointing outward, and $m_{V(t)}$ is the enclosed mass. The surface element $\mathrm{d}\vec{S}$ can be written as $\mathrm{d}\vec{S} = \vec{n}\ \mathrm{d}S$. The quantities $\rho(\vec{x},t)$ and $\vec{v}(\vec{x},t)$ are density and velocity of the fluid at time t and position $\vec{x}$.

In a duct, the mass flow out of a control section is limited through the surrounding walls and flow in and out of the fixed (i.e. $\vec{w}(\vec{x},t) = 0$) CR is only possible at the fixed inlet and outlet surfaces $A(x_1)$ and $A(x_2)$. Since for all following considerations, the two surfaces are chosen to be normal to the axis of the pipe, we are only interested in the axial component u of the flow velocity: $[\vec{v}(\vec{x},t) \cdot \vec{n}(\vec{x},t)]\ \mathrm{d}S = u \cdot \mathrm{d}A$. This reduces Eq. 2.2 to

$$\frac{\mathrm{d}}{\mathrm{d}t} \int\limits_{V} \rho(\vec{x},t)\ \mathrm{d}V + \int\limits_{A(x_2)} \rho(\vec{x},t) u(\vec{x},t)\ \mathrm{d}A - \int\limits_{A(x_1)} \rho(\vec{x},t) u(\vec{x},t)\ \mathrm{d}A = 0 \quad . \tag{2.3}$$

A useful and valid approximation in pipe flows is the assumption of constant density over the cross section $A(x)$ of the conduit and to furthermore introduce the cross sectionally averaged velocity $U(x,t) = \frac{1}{A(x)} \int_{A(x)} u(\vec{x},t)\ \mathrm{d}A$ in the axis direction x. This allows to write the continuity equation in its differential form

$$\frac{\partial}{\partial t}(\rho A) + \frac{\partial}{\partial x}(\rho A U) = 0 \quad . \tag{2.4}$$

If the control region of interest is only of short length L, in comparison to density fluctuations along the axis (e.g. traveling pressure waves), we can neglect the spatial dependence of the density entirely and inside the CR the density becomes a function of time only: $\rho = \rho(t)$. Under the above assumptions, the continuity equation for a fixed control region in a pipe of volume V_0 with equal front and back boundary surfaces ($A(x_1) = A(x_2) = A$) can be expressed as

$$\begin{aligned} &\frac{\partial\rho}{\partial t}V_0 + \rho A U_2 - \rho A U_1 = \\ &\qquad \frac{\partial\rho}{\partial t}V_0 + J_2 - J_1 = 0 \quad . \end{aligned} \tag{2.5}$$

With $J_{1,2}(x,t) = \rho(t)\ A\ U_{1,2}(x,t)$, the mass flow into the CR at boundary 1 or 2, respectively.

2.2.2. Momentum Equation

In analogy to the above derivation of the mass balance in a conduit, we can derive the momentum equation for the arbitrary CR. The rate of change of momentum in the volume $V(t)$, plus the momentum that is convected into the region across its boundary, has to balance the external forces:

$$\begin{aligned} \frac{\mathrm{d}}{\mathrm{d}t}\int\limits_{V(t)} \rho(\vec{x},t)\vec{v}(\vec{x},t)\ \mathrm{d}V + \oint\limits_{\partial V(t)} \rho\vec{v}(\vec{x},t)\big[\big(\vec{v}(\vec{x},t) - \vec{w}(\vec{x},t)\big)\cdot\vec{n}\big]\ \mathrm{d}S \\ = \sum \vec{F}_{ext}(t) \quad , \end{aligned} \tag{2.6}$$

as stated in [6, 7, 8]. Here the external forces include all fluid-solid surfaces, fluid-fluid surfaces and all forces applied to the fluid volume. For horizontal CRs of short length we can neglect gravitational forces and therefore volume forces can be set to zero. Fluid-fluid surface forces include pressure forces normal to the boundaries $\left(-\int_{\partial V_{fluid}} \vec{n}\cdot p(x,t)\ \mathrm{d}S\right)$ and viscous forces acting in all directions. Fluid-solid surfaces include friction forces between the fluid and the walls or any solid obstacle, like an orifice plate. If we now view the momentum transport equation for a horizontal conduit of length $\delta x \to 0$, using the above definitions and simplifications made for the continuity equation and the external forces, we can rewrite Eq. 2.6 to

$$\frac{\partial}{\partial t}\int\limits_A \rho u \,\mathrm{d}A + \frac{\partial}{\partial x}\int\limits_A \rho u^2 \,\mathrm{d}A = -\int\limits_A \frac{\partial p}{\partial x}\,\mathrm{d}A + f_{viscous} + f_{wall} \quad , \tag{2.7}$$

where the viscous and wall shear forces have been labeled $f_{viscous}$ and f_{wall}, respectively. Those will be considered in detail later on.

Again setting the density spatially constant in the CR and using an averaged pressure gradient for the cross section A, allows to write the momentum equation for a pipe in its differential form:

$$\boxed{\frac{\partial}{\partial t}(\rho A U) + \frac{\partial}{\partial x}(\beta_m \rho A U^2) = -A\frac{\partial p}{\partial x} + f_{viscous} + f_{wall} \quad . \qquad (2.8)}$$

β_m is the momentum correction coefficient defined by $\beta_m = \frac{1}{A}\int_A \frac{u^2}{U^2}\,\mathrm{d}A$, to take into account the deviations of the actual profile $u(\vec{x},t)$ from the cross sectionally averaged velocity profile $U(x,t)$. This β_m should not be mistaken for the commonly used β, which characterizes the orifice to pipe ratio and will be labeled β_d from here on.

For later reference, one final modification of the momentum equation is made. Using the continuity equation 2.4 and basic laws of differentiation, the momentum equation can be rewritten in the nonconservative form:

$$\rho A\frac{\partial U}{\partial t} + \rho A U\frac{\partial U}{\partial x} + \frac{\partial}{\partial x}\left[(\beta_m - 1)\rho A U^2\right] = -A\frac{\partial p}{\partial x} + f_{viscous} + f_{wall} \quad . \tag{2.9}$$

2.2.3. Streamlines and Streamtubes

In the later discussion about steady flow metering equations, the concept of streamlines and streamtubes is applied, which is why their definitions should be briefly mentioned at this point. A streamline in a continuous flow field is defined as a line that at any instant t is tangent to the velocity of the flow field [6]. This line therefore indicates the instantaneous direction of the velocity of the fluid particles on it. Since in steady flow the velocity field does not change in time, the streamlines in steady flow are also the paths of the fluid particles.

A set of adjacent streamlines forming a tube is called a stream surface or streamtube. Streamtubes are often used in discussions about orifice meters and pipes in general, since the pipe wall can be seen as a natural boundary of streamlines enclosing a streamtube.

2.3. Characterization of Pipe Flow

2.3.1. Steady Pipe Flow

A fairly important question in flow metering is the question about the velocity distribution inside the conduit, since this distribution is needed to calculate the mass flow through any cross sectional area of an orifice meter. There are mainly two flow regimes for newtonian fluids, where different velocity distributions occur: Laminar and turbulent flow [6]. Because there is no clear cut boundary between those two, a transitional region is defined that describes the transition between laminar and turbulent flow.

Fluid-wall interactions force the fluid to come to a stop at the walls of the pipe, this is called the *no-slip condition*. Shear stresses inside the fluid then only allow a gradual, radial approach to a maximum flow velocity at the pipe center. At low flow speeds, the laminar region, a fluid flows in parallel layers, resulting in a parabolic shape of the velocity distribution:

$$u(r) = u_{max} - u_{max} \left(\frac{r}{R} \right)^2 \quad , \tag{2.10}$$

as given in [7], where R is the radius of the pipe. At higher velocities random fluctuations, referred to as turbulence, occur in the velocities of the fluid particles. This leads to an additional momentum transfer in the normal direction of the main flow, allowing a steeper increase of the velocity in the vicinity of the wall. In total a more evenly distributed velocity profile can be observed, which slightly depends on fluid and pipe properties. Nevertheless an approximative definition is given e.g. in [7] by:

$$u(r) = u_{max} \left(1 - \frac{r}{R} \right)^{1/7} \quad . \tag{2.11}$$

This turbulent velocity profile is usually referred to as the 1/7-profile because of the empirical 1/7 exponent.

A useful quantity in pipe flows, to distinguish between the different flow regimes is the Reynolds number, defined by

$$\mathrm{Re} = \frac{UD}{\nu} \quad , \tag{2.12}$$

where D is the pipe diameter and ν is the kinematic viscosity of the fluid. In pipe flow, the transition from laminar to turbulent flow occurs at a Reynolds number of about 2330.

For air with a viscosity of approximately $15 \cdot 10^{-6}\ m^2/s$ and a pipe diameter of roughly 10 cm as is the case for the metering sections in this work, the transition would happen at mean flow speeds below 1 m/s. Since flow speeds encountered in engine connected ducts, most of the time are much higher, flows in this work are generally considered turbulent.

Steady Friction

The above mentioned shear stresses inside the fluid and at the fluid-wall boundary both result in forces acting against the direction of motion. In steady pipe flows these friction forces are usually described by the phenomenological Darcy-Weisbach equation (given in [7]):

$$f_{viscous} + f_{wall} = \frac{\pi D \rho f_D U|U|}{8} \quad , \tag{2.13}$$

where f_D is an empirical constant, depending on pipe wall roughness, pipe diameter and Reynolds number. When orifices are installed, losses are more complex to describe theoretically and significantly higher than in smooth pipes, due to the increased dissipation in the wakes of an orifice. This will be discussed in detail later on, but is mentioned here, as these losses, although non-negligible, are generally omitted in the derivation of orifice mass flow equations and additionally play an important role in pulsating flows.

2.3.2. Pulsating Flow

In environments that include engine intake or exhaust flows, where fast variations in pressure and in flow speed arise, the above considerations and simple descriptions for steady flow become invalid. The occurring pressure variations, which often are periodic and generally termed pulsations, alter the flow behavior and make a more detailed analysis necessary.

Strouhal and Womersley number

Two useful dimensionless quantities, that help characterizing the *unsteadiness* of pulsating flows, are the Strouhal number St and the Womersley number Ws. In the context of pulsating orifice flow they are defined by

$$\mathrm{St} = \frac{fd}{U_d} \quad , \tag{2.14}$$

$$\mathrm{Ws} = \frac{d}{2}\sqrt{\frac{f}{\nu}} \quad , \tag{2.15}$$

as given in [9, 10], where f is the characteristic frequency of the pulsation, d is the inner orifice diameter and U_d is the maximum mean velocity at the orifice. They are proportional to the ratio of local to convective acceleration and the ratio of local acceleration forces to viscous forces, respectively. In straight pipe flow, as well as in orifice flow, both quantities help to distinguish between slow, *quasi-steady*, and fast, pulsating flows, that need to be treated separately. The magnitude and importance of these quantities for air intake and exhaust gas flows will be addressed after a short illustration of the dynamics in pulsating flows.

Unsteady Flow Field

Plenty of research has been conducted on the topic of oscillating laminar flows in unobstructed pipes and channels and analytical solutions to such flows exist. Richardson [11] first described considerable differences between steady flow profiles and the ones in unsteady flow. He and other authors [12, 13] described flow profiles including off-axis maximum velocity magnitudes and reverse flow near the conduit walls for higher frequencies (Fig. 2.1). Another, perhaps more obvious consequence of the pulsating pressure, is an induced phase lag of the mean fluid velocity relative to the applied pressure gradient due to the inertia of the fluid. Phase shifts up to 90° for high frequencies can be found [14].

As mentioned before, the velocities of interest in intake and exhaust flows lie in the higher Reynolds number turbulent and transitional flow regions. Transient turbulent and transitional flows are less well-understood, but reasonable explanations of the flow effects occurring are available nonetheless (e.g. He and Jackson [15]):

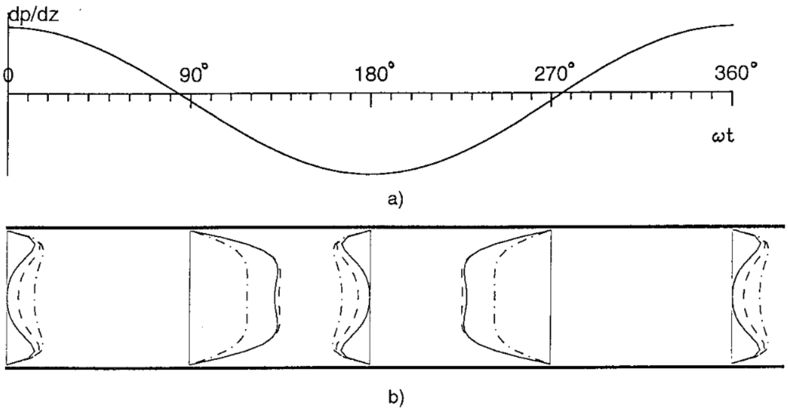

Figure 2.1.: Oscillating laminar channel flow [14]. a) Pressure gradient with respect to time. b) Velocity profiles in channel at different times in oscillation cycle.

When a pressure wave front passes at an arbitrary position in a pipe, the fluid at that cross section is instantaneously accelerated or decelerated for some small amount and the velocity profile can be imagined undergoing a small uniform shift. Because of the no-slip condition at the wall, this will generate vorticity inside the boundary layer. As a result of this process, shear waves will be created at the wall and will travel towards the center of the pipe. Dissipation will then attenuate the propagating shear waves as they are stretching into the fluid core. Uchida [13] introduced a length scale in laminar flows for the attenuation inside the fluid, giving the distance in which the shear wave is damped by a factor e. The length scale is given by the Stokes layer thickness l_s:

$$l_s = \sqrt{\frac{2\nu}{\omega}} \quad , \tag{2.16}$$

where ω is the angular frequency of the pressure oscillation. For both laminar and turbulent flow, the attenuating shear wave will produce a variable change of the velocity field inside the Stokes layer. In a distance from the wall greater than the layer thickness, the flow velocity distribution will be altered uniformly and practically behave like a *plug flow*.

Depending on the frequency of the pressure modulation, the distance that the shear waves travel will stretch out farther into the main flow. For very high frequencies, the Stokes layer will be confined to the viscous sublayer in the immediate proximity of the wall and almost all of the fluid inside the pipe behaves like a plug. Below a certain frequency, the Stokes layer starts to extend deeper into the fluid and causes the observed, variable changes in the velocity distribution as it attenuates.
When the characteristic times of the changes in one pulsation cycle start to become much smaller than the time needed for the shear wave to reach the center of the pipe, an equilibrium state can be reached at each point in time and *quasi-steady* flow behavior can be observed.

The above introduced Womersley number is inversely proportional to the Stokes layer thickness and therefore allows an assessment of the critical frequency, when pulsation effects have to be considered. For low frequencies, i.e. $\frac{1}{l_s} \propto \mathrm{Ws} \ll 1$, local acceleration forces are small in the governing momentum equation and quasi-steady flow is present. When the pulsation frequency is increased and the Womersley number reaches the order of one, i.e. the Stokes layer becomes smaller than half the pipe diameter, no equilibrium state can be reached and the flow behavior starts to deviate from the quasi-steady one.

For intake air flow with a kinematic viscosity of approximately $15 \cdot 10^{-6}\ m^2/s$ at an orifice of 5 cm inner diameter this means, that viscosity effects already start to play a role at frequencies as low as 1 Hz and certainly impact flow behavior above 10 Hz. Beyond that, local acceleration forces are balanced by the viscous terms and the additional phase shift between pressure differential and flow rate will be clearly observable. As for exhaust gas flows, the increase of viscosity with temperature slightly raises the critical frequency, but no significant differences should be present.

Unsteady Friction

To account for viscosity losses in unsteady pipe flows, initially the phenomenological Darcy-Weisbach equation (Eq.2.13) has been applied [8]. This approach can lead to a significant underestimation of the friction when the frequencies of the pressure changes lie in the above mentioned domain, where major deviations of the flow field from a steady one are induced. For example when mean flow is zero, the Darcy-Weisbach friction would give zero friction. In a transient flow however, zero mean flow can be reached with a positive flow velocity in the core of the pipe and flow reversal at the wall. These flow situations will cause particularly high dissipation rates in smooth pipes as in orifices, because of the large velocity gradients and the accompanied large shear stresses.

Several different methods have been introduced to account for the higher resistance coupled with the unsteadiness of the flow. Convolution based methods as reviewed in [8] in the form of

$$f_{viscous} + f_{wall} = f_{steady} - \frac{\nu\rho}{A}\int\limits_0^t W(t-t')\frac{\partial U}{\partial t'}\,\mathrm{d}t' \quad , \tag{2.17}$$

are computationally extensive and rely on the weighting coefficients W from analytical solutions, that are not available for orifices. Simpler models are the instantaneous acceleration based models, which were first considered for orifices by Daily et al. [16]. They used a control region approach applied to orifices and smooth pipes and introduced an unsteady friction coefficient k, which relates the instantaneous acceleration $\partial U/\partial t$ with the additional unsteady friction:

$$f_{viscous} + f_{wall} = f_{steady} - k\rho A\frac{\partial U}{\partial t} \quad , \tag{2.18}$$

where f_{steady} denotes the steady friction part. Some corrections to this model have been made by Brunone [17] and Bergant [18]. These corrections include the convective acceleration to introduce higher friction when the flow is being accelerated and lower friction when the flow is being decelerated, delivering accurate dissipation results for fast transients in smooth pipes:

$$f_{viscous} + f_{wall} = f_{steady} - k\rho A \left(\frac{\partial U}{\partial t} + c \ \mathrm{sgn}(U) \left| \frac{\partial U}{\partial x} \right| \right) \quad , \tag{2.19}$$

where c is the velocity of sound.

Because the inclusion of the convective acceleration term in an unsteady friction ansatz for orifice flow would inevitably imply the need for an additional calibration constant, the instantaneous acceleration based model of Daily et al. in the form of equation 2.18 will later be applied in the derivation of an orifice mass flow equation for pulsating flows.

2.4. Steady Orifice Flow

All above considerations about steady and unsteady flows in the following will be applied to review the principles of steady and unsteady flow measurement with the use of orifice meters.

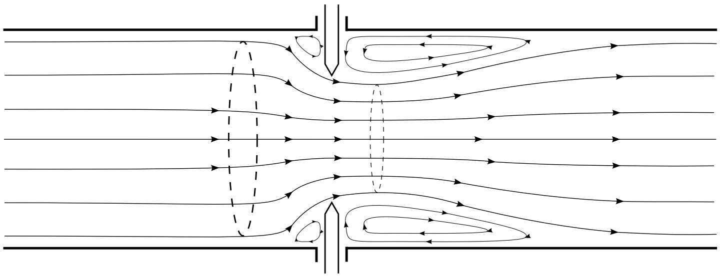

Figure 2.2.: Sketch of the streamlines and a streamtube in steady flow through an orifice.

When considering steady and, also expanding this analysis to the turbulent region, statistically steady flow, the density and flow velocity become independent of time.

Thus the terms $\frac{\partial}{\partial t}(\rho A)$ in the continuity equation 2.4 and $\frac{\partial U}{\partial t}$ in the momentum equation 2.9 become zero. Additionally making the simplifications of assuming a uniform velocity profile, i.e. setting $\beta_m = 1$, and neglecting friction, the resulting momentum balance reads:

$$\rho U \frac{\partial U}{\partial x} = -\frac{\partial p}{\partial x} \quad . \tag{2.20}$$

Further assuming incompressible flow allows to restate this relation in a form, where it is known as the Bernoulli equation, valid for a horizontally running streamline:

$$\frac{\partial}{\partial x}\left(\frac{1}{2}\rho U^2 + p\right) = 0 \quad . \tag{2.21}$$

Simply integrating the Bernoulli equation over the length of the restriction of the metering device gives:

$$\frac{1}{2}\rho(U_2^2 - U_1^2) + p_2 - p_1 = 0 \quad , \tag{2.22}$$

where the subscripts 1 and 2 are the positions of the pressure tappings upstream and downstream of the restriction, respectively. Using the continuity equation for steady flow,

$$J = \rho A_1 U_1 = \rho A_2 U_2 \quad , \tag{2.23}$$

which merely states the fact that for incompressible flow, the flow into the control region has to equal the flow out of the control region, allows to eliminate the unknown flow velocities U_1 and U_2 in the above result, Eq. 2.22. Additionally combining the two pressure variables into one pressure difference, $\Delta p = p_1 - p_2$, will lead to

$$J = \frac{1}{\sqrt{1/A_2^2 - 1/A_1^2}} \sqrt{2\rho\Delta p} \quad , \tag{2.24}$$

for the mass flow J. In many illustrations this is further reduced to

$$J = \frac{A_2}{\sqrt{1 - (A_2/A_1)^2}} \sqrt{2\rho\Delta p} \quad . \tag{2.25}$$

2.4.1. Flow Meter Equation

Equation 2.25 only applies to idealized one-dimensional flow and neglects certain characteristic attributes of real fluid flow through the orifice. To improve its applicability, some considerations about the flow inside the flow meter have to made.

Contraction Coefficient

The utilization of streamlines and a fixed uniform velocity profile in the above derivations, basically defines a streamtube passing through the orifice. This streamtube rather abruptly contracts approaching the orifice and gradually recovers in cross section after passing through, as is sketched in Fig. 2.2. An important feature of this streamtube, is the prolonged contraction of the stream behind the orifice, due to the radially inward pointing inertia of the outer fluid particles. This effect is commonly known as the *vena contracta effect*.

The concept of a streamtube carrying along the cross sectional averaged fluid mass and momentum requires the additional declaration of the cross sections A_1 and A_2 of this tube, which in general are not equal to the pipe diameter. Usually this problem is addressed by the introduction of a velocity dependent contraction coefficient C_C, that relates the tubes cross section to the pipes cross section:

$$A_{tube} = C_C A_{pipe} \quad . \tag{2.26}$$

Since the flow upstream of the orifice should be undisturbed laminar or turbulent flow, the diameter of the streamtube at the upstream pressure tapping is set to the diameter of the pipe and therefore $A_1 = \pi D^2/4$. One has to be aware of the fact, that this assumption becomes more inaccurate, the further the upstream tapping is moved towards the orifice plate, because of the inward bending of the streamlines and possible vortices prior to the obstruction. The downstream streamtube cross section is most commonly related to the orifice diameter, $A_2 = C_C \pi d^2/4$, resulting in the following mass flow equation:

$$J = \frac{\pi d^2}{4} \frac{C_C}{\sqrt{1 - C_C^2 \beta_d^4}} \sqrt{2\rho\Delta p} \quad , \tag{2.27}$$

with $\beta_d = d/D$, the ratio of orifice to pipe diameter. If one would consider the contraction upstream of the orifice, the two effective contraction coefficients labeled C_C would be different.

Velocity Coefficient

Another feature not considered in the above derivation is the non-uniformity of the cross sectional velocity profile in real flows and the implicated uneven distribution of energy and momentum across the stream. This can be accounted for in the integrated Bernoulli equation, Eq. 2.22, by the use of energy correction coefficients $\alpha = 1/A \int_A u^3/U^3 \, \mathrm{d}A$, similar to the momentum correction coefficients β_m. Taking these corrections into account will lead to

$$J = \frac{\pi d^2}{4} \frac{C_C}{\sqrt{\alpha_2 - \alpha_1 C_C^2 \beta_d^4}} \sqrt{2\rho \Delta p} \quad . \tag{2.28}$$

In an attempt to simplify this relation, one velocity coefficient C_V is used in place of the two energy correction coefficients:

$$J = \frac{\pi d^2}{4} \frac{C_C C_V}{\sqrt{1 - C_C^2 \beta_d^4}} \sqrt{2\rho \Delta p} \quad , \tag{2.29}$$

with

$$C_V = \sqrt{\frac{1 - C_C^2 \beta_d^4}{\alpha_2 - \alpha_1 C_C^2 \beta_d^4}} \quad . \tag{2.30}$$

Expansibility Coefficient

Up to this point the flow has been assumed incompressible. Since real fluids, especially gaseous media, are compressible, one has to account for variable density. This is done, by the use of a so called expansibility coefficient ε, which is simply introduced as a multiplicative factor into the mass flow equation:

$$J = \frac{\pi d^2}{4} \frac{\varepsilon \, C_C C_V}{\sqrt{1 - C_C^2 \beta_d^4}} \sqrt{2\rho \Delta p} \quad . \tag{2.31}$$

It should be noted that this coefficient is presumed not to depend on Reynolds number, but only on the isentropic exponent of the fluid and the static pressure [19, 20]. Hence it only corrects for deviations in the mass flow due to static pressure variations.

Discharge Coefficient

It is obvious that the above form of the mass flow equation, Eq. 2.31, is inconvenient for practical use, as it is difficult to identify and measure the different coefficients. For this reason, the contraction and velocity coefficients are combined to the discharge coefficient C_D:

$$\boxed{J = \frac{\pi d^2}{4} \frac{\varepsilon \, C_D}{\sqrt{1-\beta_d^4}} \sqrt{2\rho \Delta p} \quad .} \tag{2.32}$$

This is the well established steady flow meter equation as it is used in many devices. Discharge and expansibility coefficients are usually determined by calibration or by empirical equations, which exist for many different obstruction geometries and configurations. Coefficient values for conventional orifice and venturi geometries can for example be found in the ISO standard ISO 5167, where the discharge coefficient is given by the Reader-Harris/Gallagher equation as a function of the Reynolds number, calculated with respect do the pipe diameter D [21]:

$$\begin{aligned} C_D =& 0.5961 + 0.0261\beta_d^2 - 0.216\beta_d^8 + 0.000521\left(\frac{10^6\beta_d}{\mathrm{Re}_D}\right)^{0.7} \\ &+ (0.0188 + 0.0063\left(\frac{19000\beta_d}{\mathrm{Re}_D}\right)^{0.8})\beta_d^{3.5}\left(\frac{10^6}{\mathrm{Re}_D}\right)^{0.3} \\ &+ (0.043 + 0.08e^{-10L_1} - 0.123e^{-7L_1})(1 - 0.11\left(\frac{19000\beta_d}{\mathrm{Re}_D}\right)^{0.8})\frac{\beta_d^4}{1-\beta_d^4} \\ &- 0.031\left(\frac{2L_2}{1-\beta_d} - 0.8\left(\frac{2L_2}{1-\beta_d}\right)^{1.1}\right)\beta_d^{1.3} \quad , \end{aligned} \tag{2.33}$$

where L_1 and L_2 are the quotients of the distances of the pressure tappings from the respective orifice faces and the pipe diameter.

2.4.2. Permanent Pressure Loss

Up to this point, friction losses have been disregarded in the steady orifice flow analysis. Installing an orifice plate in a pipe produces an increased pressure loss in the pipe, because of the additional dissipation around the orifice. The total, permanent pressure loss, i.e. the pressure difference one would measure upstream (usually $\approx D$) and downstream ($\approx 6D$) of the orifice plate at distances where the flow is not directly affected by the orifice anymore, is given in the ISO standard ISO 5167-1 [19]. A friction coefficient in analogy to the Darcy-Weisbach equation is defined by

$$K = \frac{\Delta\varpi}{\frac{1}{2}\rho U|U|} = \left(\frac{\sqrt{1-\beta_d^4(1-C_D^2)}}{C_D\beta_d^2} - 1 \right)^2 \quad , \tag{2.34}$$

where $\Delta\varpi$ is the permanent pressure loss. An approximate value of $\Delta\varpi$ can be calculated by $\Delta\varpi = (1-\beta_d^{1.9})\Delta p$. With a diameter ratio of $\beta_d = 0.7$ the pressure loss would amount to about half the measured pressure difference. Even though it is difficult to make a statement about the distribution of the pressure loss over the measured distance, this shows that frictional losses should be accounted for in theory and could introduce an additional error in unsteady measurement.

2.5. Unsteady Orifice Flow

In the section about pulsating flow, some features of unsteady, oscillating flows in circular pipes have already been discussed. Below, the common approaches to deal with unsteady behavior in orifice flow and to measure unsteady mass flow rates are reviewed.

2.5.1. Quasi-Steady Theory

In the derivations for the equation of steady orifice flow, Eq. 2.32, the temporal acceleration term $\frac{\partial U}{\partial t}$ in the momentum equation was set to zero. This of course is not justifiable for unsteady flow. It is permissible though, to neglect the temporal acceleration under the assumption that it is small in comparison to the convectional acceleration term at the metering section [1, 22].

$$\mathrm{St} \approx \frac{\frac{\partial U}{\partial t}}{U\frac{\partial U}{\partial x}} \ll 1 \tag{2.35}$$

A closer analysis of the ratio of accelerations by several authors [23, 24] has shown, that this ratio is closely linked to the afore mentioned Strouhal number St. As a logical consequence, disregarding the temporal acceleration term will only yield acceptable results for very low frequencies or high pulsation amplitudes.

Inertial Error

Using the quasi-steady assumption and therefore neglecting inertial effects of the fluid flow will lead to deviation in the flow rate called *inertial error*. Because of its inertance, a moving or resting fluid will always try to stay in its previous state. This results in the above described phase lag between pressure and flow rate for pulsating flow. The measured pressure difference therefore can not directly be connected to the momentary flow rate. Using the quasi-steady theory would result in overestimating accelerated flow rates and underestimating decelerated flow rates.

Additional sources of error in the quasi-steady assumption, are the flow coefficients in Eq. 2.32. Such errors commonly are referred to as residual errors and stem from the fact, that using coefficients determined for steady flow measurements would implicate the same flow behavior in pulsating flows [22]. This of course is not the case for higher frequencies and large amplitudes in comparison to the

mean flow:
It has been stated previously by several authors [16, 25, 26] that the flow profile at an orifice under these conditions, drastically deviates from a steady one. The reason for this behavior is the recirculation region that is formed downstream of the orifice. Fluid in the recirculation region is flowing radially inwards at the orifice plate and will first be accelerated in the reverse direction in a deceleration phase. This leads to a pronounced annular effect and will occur well before the main, core flow would reverse its direction (see Fig.2.3).

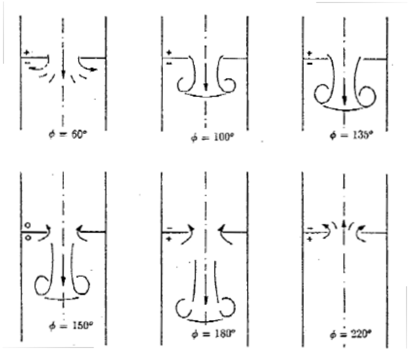

Figure 2.3.: Sketch of flow directions at an orifice at different phases ϕ of an oscillation cycle [26].

Square Root Error

Another well documented source of error, while applying the steady flow equation to pulsating flow, is the so called square root error [27, 28]. This error refers to the deviation of the calculated mean mass flow from the actual mass flow, which is introduced because of the nonlinear relation between mass flow and the measured differential pressure. As a result of the nonlinear relation, the mean of the measured differential pressure will not be equal to the differential pressure belonging to the mean mass flow of a pulsating flow. This will cause an overestimation of the mean flow rate. It is illustrated in Fig. 2.4a.

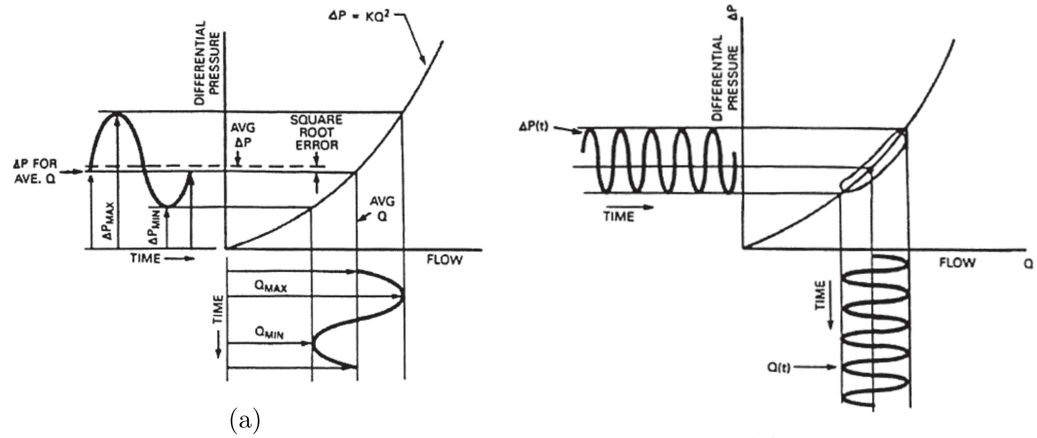

(a)

(b)

Figure 2.4.: Illustrations of (a) square root error effect and (b) inertial error effect. K here is the calibration constant [27].

2.5.2. Temporal Inertia Theory

Some crucial improvements to the quasi-steady theory have been made by allowing for and incorporating the temporal acceleration into the measurement equations. Still assuming incompressibility, including the unsteady term $\frac{\partial U}{\partial t}$ before integrating Eq. 2.20 along the obstruction length will yield

$$\Delta p = J^2 \frac{1 - C_C^2 \beta_d^4}{2\rho (C_C \varepsilon \pi d^2/4)^2} + \rho \int_1^2 \frac{\partial U}{\partial t} \, \mathrm{d}x \quad , \tag{2.36}$$

for the instantaneous differential pressure. The last term containing the integral cannot be evaluated without making some further modifications. Using the continuity equation and arbitrarily splitting the temporal and spatial dependency, i.e. $J(t) = \rho A(x) U(x,t)$, will result in

$$\Delta p = J^2 \frac{1 - C_C^2 \beta_d^4}{2\rho (C_C \varepsilon \pi d^2/4)^2} + \frac{\partial J}{\partial t} \int_1^2 \frac{1}{A(x)} \, \mathrm{d}x \quad . \tag{2.37}$$

Since the dependency of the cross section along the integral path is not known, it is customary to apply the concept of an effective length L_ε, first introduced by Mottram [1]. In analogy to his derivations for venturi tubes, he replaced the integral by an empirical constant corresponding to the acoustic inertance of the orifice:

$$\int_1^2 \frac{1}{A(x)}\,\mathrm{d}x = \frac{L_\varepsilon}{C_C \frac{\pi d^2}{4}} \quad , \tag{2.38}$$

where L_ε is a characteristic length, which depends on the shape and geometry of the obstruction and is in the order of the diameter d of the restriction. From a physical viewpoint the whole last term in Eq. 2.37 describes the additional instantaneous pressure difference needed to accelerate the fluid at current mass flow J. There are several different approaches to determine the actual value of the effective length, but the underlying problem is to empirically assess the flow dependent coefficients $A(J(t),t)$ and $B(J(t),t)$ in the nonlinear differential equation

$$\Delta p = \frac{A}{\rho} J^2 + B \frac{\partial J}{\partial t} \quad , \tag{2.39}$$

see for example [29, 30]. Various authors have carried out studies, both experimental and numerical, to find an acceptable approximation for the effective length L_ε as part of estimating the coefficient B [29, 31]. However, the success of the particularly chosen values appeared to be strongly depending on the main frequency component of the pulsating flow and whether reverse flow occurred in the measurements. The considerable error dependence on the flow situation can, to a certain extent, be attributed to the differing flow profiles in pulsating flow, compared to the assumed steady flow profiles in the calculations. Because of these inconsistencies, no definite recommendations for the constant B can be found and Doblhoff-Dier [29] even suggested the restriction of the applicability of Eq. 2.39 to small ratios of the pulsation amplitude $\widetilde{U}$ to the frequency times orifice diameter, i.e. fd. This is a similar demand like the one for small Strouhal number made by Mottram for the applicability of the quasi-steady theory. All the above underlines the assumption, that B is not a geometry dependent constant, but rather a flow dependent variable.

Once again recalling the Womersley number, it should be noted at this point, that the dependence of the Womersley number on the orifice diameter suggests, that a reduced diameter would directly decrease the unsteady flow effects. For a constant orifice to pipe area ratio, this can be achieved by using a multi-hole orifice-plate, where each individual hole diameter is considerably smaller than the single orifice diameter.

2.6. Acoustics

In addition to the flow effects at the orifice, it is crucial to examine the pressure measurement system that transfers the pressure from the pressure tappings at the orifice to the pressure transducers. Acoustic effects therein, like resonances, will inevitably introduce considerable errors to the flow measurement.
Moreover, acoustic resonances will be deliberately applied in the experimental investigation with a resonance pipe, since they present a well defined environment for pulsation measurement.

2.6.1. Acoustic Impedance

A useful quantity in the following discussion is the specific acoustic impedance, which is defined as the ratio of pressure p to the resulting particle velocity U [32]:

$$z = \frac{p}{U} \quad . \tag{2.40}$$

Using the linearized momentum equation, the characteristic acoustic impedance of a one-dimensional plane wave in a pipe of cross section A then is

$$Z_0 = \frac{p}{UA} = \frac{\rho_0 c}{A} \quad , \tag{2.41}$$

where ρ_0 is the density of the air, c the speed of sound and p and U are the amplitudes of pressure and cross sectionally averaged particle velocity of the plane wave, respectively. The relation between pressure and velocity amplitude in equation 2.41 can be used to estimate the amplitude of the flow velocity in a pipe, when the pressure amplitude is measured.

2.6.2. Resonance Behavior

The gauge lines connecting the pressure transducers can be approximately viewed as a tube rigidly terminated at the end of the transducer and open ended at the tappings, forming the same basic but reversed structure as a resonance pipe with a rigid acoustic driver at one end. If such pipes are acoustically driven by a mechanical input impedance $Z_i = Force/U$ at frequencies for which only plane waves will propagate, i.e. wavelengths are considerably longer than radial extensions of the pipe, the pressure inside the pipe can be described by forward (p_+) and backward (p_-) traveling plane waves [32]:

$$p(x,t) = p_+ e^{j[\omega t + k(L-x)]} + p_- e^{j[\omega t - k(L-x)]} \quad , \tag{2.42}$$

where j is the imaginary unit, $k = 2\pi/\lambda$ is the wavenumber and L is the total length of the pipe. The particle velocity is given by the momentum equation, using acoustic assumptions:

$$U(x,t) = -\frac{1}{\rho_0}\int_0^t \frac{\partial p(x,t')}{\partial x}\,\mathrm{d}t' \quad . \tag{2.43}$$

The impedance of the waves in the pipe, Z_0, is given by Eq. 2.41. Neglecting damping and approximating the mechanical impedance of the rigid end with infinity, the input impedance for plane waves in the pipe is given by [32]

$$Z_i/Z_0 = -j\cot(kL) \quad . \tag{2.44}$$

When $\cot(kL)$ becomes zero, the velocity amplitude U at the point of application of the input impedance becomes infinite and resonance (maximum amplitude) occurs. The condition for $\cot(kL) = 0$ and hence resonance is

$$L = (2n-1)\frac{\lambda}{4} \qquad \text{with} \quad n = 1, 2, 3, ... \tag{2.45}$$

These resonances will occur when the quarter wavelength is an odd multiple of the pipe length and are termed *standing waves*, since amplitudes are constant at each point in the pipe. The resulting in pressure maxima p and particle velocity maxima U are displaced by a quarter wavelength and hence pressure nodes are located at velocity antinodes. Because there is sound radiated into the surrounding medium at the open end, there has to be made a minor correction for the impedance at the open end. When the resonance pipe is circular and cylindrical at the open end, this correction results in a slightly longer effective length of the pipe and is called end correction: $L_{eff} = L + 0.85R$, where R here is the radius of the pipe [32].

In the case of the connection tubes of the pressure measurement system used in this work, which are approximately of 0.25 m length, the fundamental ($n = 1$) of the resonance modes is located at approximately 340 Hz.

This is not the only resonance behavior that has to be taken into account for the pressure measurement system. The combined system of gauge lines and transducer inner volumes will act as a Helmholtz resonator when excited with an oscillating pressure from the outside. Compressible fluid inside a volume can be considered a spring, that is connected to the outside by the fluid in the gauge lines. The fluid in the tube, moving as a unit, acts as an oscillator mass. Such a system then has a Helmholtz resonance fundamental of

$$f_0 = \frac{c}{2\pi}\sqrt{\frac{A}{L(V + \frac{LA}{2})}} \quad , \tag{2.46}$$

as is shown in [32, 33], where V is the internal volume of the pressure sensor.

Doblhoff-Dier [34] already made an assessment for the pressure system in use, stating a fundamental Helmholtz resonance frequency in the order of the $\lambda/4$ - resonance. Doblhoff-Dier however neglected the influence of the additional volume that is connected to the pressure gauge lines at the tappings. There, a cylindrical channel of 1.5 cm axial extension and approximately 1 mm width spans around the whole main pipe. This introduces an additional volume of a few cubic centimeters, which is large compared to internal pipe or transducer volumes and will effectively lower the resonance frequency further. Although, because of the complex geometry, the assumption of a simple Helmholtz resonator will not be justified anymore and an accurate specification of a resonance frequency can only be given by a numerical simulation or by experiment.

3. Gas Density Determination

Rapid changes of pressure and temperature in the exhaust lines, will cause considerable fluctuations in density that have to be accounted for in the measurement process of mass flow rates. However, an exact in-flow measurement of the resulting exhaust gas density proves difficult for two reasons. Primarily, exact determination is not possible without knowing the composition of the exhaust gas, which varies with changes in the injection and combustion process. Therefore either dry air, the constituents of a stoichiometric (i.e. complete) combustion or the composition of exhaust gas at measured lambda-values (air–fuel equivalence ratio) has to be assumed. As found in previous studies by AVL GmbH [34], for complete combustion, density deviations are below ±1 % compared to air at similar conditions. During incomplete combustion, when unburnt hydrocarbons are present, deviations from air density are significantly higher and can rise to 20%.

Secondly, conventional methods usually rely on the ideal gas law, which gives good approximations for exhaust gases, to calculate densities from pressure, temperature and specific gas constant [3]. The drawback of this method is the slow dynamic response of suitable temperature measurement systems like thermocouples or resistance temperature detectors (RTD). Commercially available thermocouples with an active element of only a few micrometers could be used for unsteady temperature measurements, but do not provide the robustness needed in exhaust environments. Almost always a protecting sheath is required, which in turn produces a lag in response time. An improvement on assessing transient exhaust gas temperatures are two thermocouple probe (TTP) techniques, where the response of thicker wires is improved by using two thermocouples with different time constants at the same time and reconstructing the input signal of the sensors [35, 36]. These methods, however, are highly susceptible to noise in the temperature signal and will only provide accurate results, when the signals of both thermocouples are well distinguishable. This is the case when temperature changes are fast and high enough, that the differing dynamic responses create a measurable temperature difference between the two thermocouples that is well beyond the noise level.

An enhancement to density measurement, can be made when considering the near-adiabatic nature of changes of the gas state inside the exhaust and intake lines. The method introduced below uses the reconstructed gas temperature signal of a two thermocouple probe and the fast signal of the pressure sensor to reproduce the input temperature signal, assuming adiabatic changes of state for variations of temperature.

3.0.3. Temperature Measurement

The rate of storage of heat q_p of a wire element of a temperature sensor is equal to the heat transfer rates into the the wire through heat convection q_c, conduction q_k and radiation q_r [37]:

$$q_p = q_k + q_c + q_r \quad . \tag{3.1}$$

It can bee shown that heat transfer through the latter two can be neglected when using long and fine wires to minimize axial heat conduction and radiation [36, 35]. Looking at the rates in detail one gets

$$q_p = \rho_w c_w \frac{\partial T_w}{\partial t} \frac{\pi d_w^2}{4} \quad , \tag{3.2}$$

for the thermal inertia and

$$q_c = \frac{\mathrm{Nu}k_g}{d_w}(T_g - T_w)\pi d_w \quad , \tag{3.3}$$

for the convective heat transfer. Where the following symbols were used:

ρ_w	density of the wire
c_w	specific heat of the wire
T_w	wire temperature
T_g	gas temperature
d_w	wire diameter
Nu	Nusselt number of the gas
k_g	thermal conductivity of the gas

Neglecting heat conduction and radiation, the balance equation can be rewritten as

$$\boxed{T_g = T_w + \tau \frac{\mathrm{d}T_w}{\mathrm{d}t} \quad , \qquad (3.4)}$$

introducing the time constant of the wire

$$\tau = \frac{\rho_w c_w d_w^2}{4\mathrm{Nu}k_g} = \frac{\rho_w c_w d_w}{4h} \quad , \tag{3.5}$$

where h is the convective heat-transfer coefficient. The first order ordinary differential equation 3.4 describes the dynamic temperature response of the wire to a change in temperature of the surrounding gas. This behavior of the wire temperature can also be viewed as a low-pass filter, damping all fast temperature fluctuations of the measured gas:

$$T = \overline{T} + \tau \frac{\mathrm{d}\overline{T}}{\mathrm{d}t} \quad , \tag{3.6}$$

with $\overline{T} = T_w$, the filtered temperature signal. From the dependence of τ on the Nusselt number, which generally is a complicated function of the Reynolds and Prandtl number [38], it is clear, that the time constant itself will vary in fluctuating flow conditions, i.e. varying flow velocity, temperature, etc. So for all practical purposes one either has to a priori determine a mean time constant experimentally or calculate the time constant in situ with a suitable method.

Two Thermocouple Compensation Method

This subsection is an alternate application of the two thermocouple compensation technique first discovered by Pfriem [39] and advanced by Hung et al. [35, 40] in recent years.

When two thermocouples are assumed in close proximity and therefore are subjected to the same flow conditions, i.e. gas temperature and velocity, the dynamic behavior of two thermocouple, Eq. 3.4, can be described by the following system, where discrete time steps of sampling time t_s with constant temperature for each time step are assumed [35, 40]:

$$\begin{aligned} T_1[n] &= a_1 T_1[n-1] + b_1 T_g[n] \quad , \\ T_2[n] &= a_2 T_2[n-1] + b_2 T_g[n] \quad , \qquad (3.7) \\ a_{1,2} &= exp\left(-\frac{t_s}{\tau_{1,2}}\right) \quad , \qquad (3.8) \\ b_{1,2} &= 1 - a_{1,2} \quad . \qquad (3.9) \end{aligned}$$

To make a more general analysis of the time constant at any instance, starting from system 3.7, one can eliminate the gas temperature T_g to result in the difference equation

$$\Delta T_2^n = \beta_\tau \Delta T_1^n + b_2 \Delta T_{12}^{n-1} \qquad \text{with} \begin{cases} \Delta T_i^n = T_i^n - T_i^{n-1} \\ \Delta T_{ij}^{n-1} = T_i^{n-1} - T_j^{n-1} \end{cases} , \tag{3.10}$$

where $\beta_\tau = b_2/b_1$. This is essentially a two-variable linear optimization problem $\vec{y} = X \cdot \vec{\theta}$ for the parameters β_τ and b_2 for a given number of measurement points:

$$\mathbf{\Delta T_2^n} = [\mathbf{\Delta T_1^n}\ \mathbf{\Delta T_{12}^{n-1}}]\ [\beta_\tau\ b_2]^T \tag{3.11}$$

One can perform a simple least squares fit $\vec{\theta} = (X^T\vec{y})/(X^TX)$ to obtain a parameter estimate for a given set of data. When the parameter estimate for b_2 and $b_1 = b_2/\beta_\tau$ has been found, it is possible to reconstruct the input temperature signal from Eq. 3.7.
Previous research showed, that this estimate is highly sensitive to noise in the temperature signal, because the magnitudes of the differences in Eq. 3.10 have to surpass noise-levels for a valid parameter estimate. A more sophisticated approach using generalized total least squares (GTLS), allowing for noise on both input variables can be used to reach a less noise susceptible solution.

As the faster thermocouples employed in this work still have response times of approximately $0.5 - 1\ s$ with signal noise levels of $\sigma = \pm 0.3\ K$, this approach can only be used to enhance temperature measurement, when characteristic times of temperature changes are in the order and below the cutoff-frequency of $f_c = 1/2\pi\tau = 0.3\ Hz$ [41] and measurable temperature changes are significantly higher than twice the signal noise-level. Additionally it is advisable to artificially enlarge sampling times for oversampled temperature measurements, for a less noise-susceptible calculation of the differences $\Delta T_i^n = T_i^n - T_i^{n-1}$.

3.0.4. Adiabatic Calculation of Density

As mentioned above, an additional improvement to density measurement can be made by considering nature of changes of state of the intake or exhaust gas. Compressible gas flow in short pipes and at higher flow rates, to a first approximation can be modeled adiabatic, as heat losses are minor [42, 3]. Therefore, changes in density and temperature arising from the propagating pressure pulsations, generated by an engine, will follow the relations for an adiabatic process:

$$\rho = \left(\rho_0 p_0^{-\frac{1}{\kappa}}\right) p^{\frac{1}{\kappa}} \quad , \tag{3.12}$$

$$T = \left(T_0 p_0^{\frac{1}{\kappa}-1}\right) p^{1-\frac{1}{\kappa}} \quad , \tag{3.13}$$

where the subscript “0” is being used to denote a fixed, but arbitrary reference state.

Measuring the temperature (Eq. 3.13) of the gas with an ordinary thermocouple or RTD, as discussed above, gives a first order low-pass filtered temperature signal:

$$\overline{T} = \left(T_0 p_0^{\frac{1}{\kappa}-1}\right) \overline{p^{1-\frac{1}{\kappa}}} \quad , \tag{3.14}$$

where $\overline{p^{1-\frac{1}{\kappa}}}$ is the function $p^{1-\frac{1}{\kappa}}$ filtered with the same time constant as the temperature signal. If we now replace the reference temperature using the ideal gas law,

$$T_0 = \frac{p_0}{R_s \rho_0} \quad , \tag{3.15}$$

for a gas with the specific gas constant R_s, we arrive at

$$\overline{T} = \left(\frac{p_0}{R_s\rho_0} p_0^{\frac{1}{\kappa}-1}\right)\overline{p^{1-\frac{1}{\kappa}}} = \left(\frac{p_0^{\frac{1}{\kappa}}}{R_s\rho_0}\right)\overline{p^{1-\frac{1}{\kappa}}} \quad . \tag{3.16}$$

Rewriting this equation for the combination of reference values needed for the calculation of a density change in an adiabatic process,

$$\rho_0 p_0^{-\frac{1}{\kappa}} = \frac{1}{R_s\overline{T}}\overline{p^{1-\frac{1}{\kappa}}} \quad , \tag{3.17}$$

and actually inserting it into Eq. 3.12, one obtains a relation for the density as a function of the measured temperature and pressure:

$$\boxed{\rho(t) = \frac{p^{\frac{1}{\kappa}}}{R_s\overline{T}}\overline{p^{1-\frac{1}{\kappa}}} \quad . \qquad (3.18)}$$

This means an instantaneous density can be calculated, using an artificial filter with the same characteristics as the low-pass filter of the temperature sensors, applied to the fast pressure signal.

Example calculation results on the combination of the two-thermocouple technique and the correction based on the adiabatic assumption are plotted in figures 3.1 and 3.2. Two thermocouple signals were constructed from digitally filtering ($\tau_1 = 1\ s$, $\tau_2 = 2\ s$) an exhaust temperature signal of a two stroke engine simulated with AVL BOOST, exhibiting two discrete temperature jumps of $+100$ and $-50\ K$ at 6.9 and 13.8 s,respectively. The thermocouple signals were subsequently superimposed with normally distributed noise of $\sigma = \pm 0.3\ K$ standard deviation. Gas density then was calculated by either reconstructing the temperature with the two-thermocouple technique when the difference between thermocouple temperatures, i.e. $\Delta T_{ij}^{n-1} = T_i^{n-1} - T_j^{n-1}$, surpassed 5σ or taking the measured temperature of the thermocouple with faster response otherwise. Using Eq. 3.18 and the ideal gas law, Eq. 3.15, the temperature and density were corrected for adiabatic changes of state, where filtered values $\overline{f}_n(t)$ were calculated by Eq. 3.24 using a time constant of $\tau = 1.09\ s$. This time constant was the mean estimated by the TTP-method.

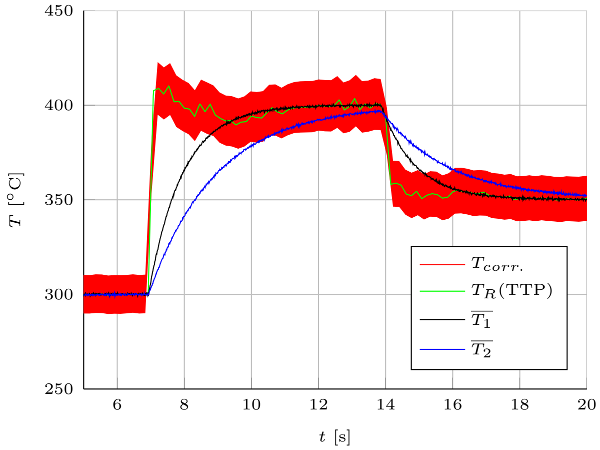

Figure 3.1.: Calculated thermocouple responses $\overline{T_1}$ ($\tau = 1\ s$) and $\overline{T_2}$ ($\tau = 1\ s$) for the exhaust of a two stroke engine simulated with AVL BOOST. Reconstructed temperature using the TTP-method on $\overline{T_1}$ and $\overline{T_2}$ is labeled T_R. Temperature correction based on the adiabatic assumption is plotted in $T_{corr.}$.

.

Density errors could be significantly reduced using the combination of the two above discussed methods. Although the TTP-method is not capable of completely eliminating errors at the times of temperature jumps, because of the high noise levels in the used thermocouple signals. The adiabatic correction provided a great reduction of continuous density errors made by the adiabatic temperature changes from 3 % to purely noise related errors below 0.2%.

Uncertainty estimates for $\Delta\rho(\Delta\tau)$ (Eq. 3.23) with an uncertainty for the time constant $\Delta\tau = 0.5\ s$, showed that the error is significantly affected by non-adiabatic pressure changes, but the error introduced in density was generally kept below 2 %.

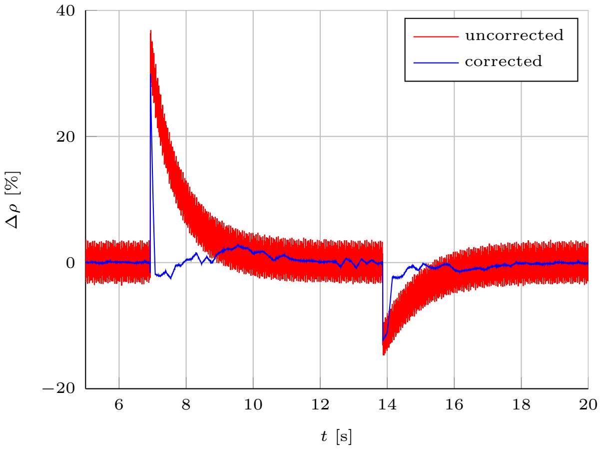

Figure 3.2.: Relative errors for calculated density when applying TTP-method together with adiabatic correction (corrected) and when calculating the density from the ideal gas law, using the faster response thermocouple temperature $\overline{T_1}$ (uncorrected).

Error Analysis

An accurate, a priori determination of the time constant of temperature sensors proves hard to accomplish, considering the sensors flow dependent nature. Therefore an error in the experimentally measured or empirically estimated time constant is inevitable. To assess the effects of any deviations of the estimated time constant on the calculated density, the accompanying error analysis should be worthwhile. The goal is to estimate the error introduced by filtering the function $p^{1-\frac{1}{\kappa}}(t)$ with a different time constant than the time constant given by the temperature measurement.

Starting from the solution of the differential equation of the filter function (Eq. 3.6)

$$\overline{f}(t) = \frac{1}{\tau} \int\limits_{-\infty}^{t} f(t') e^{-(t-t')/\tau} \, \mathrm{d}t' \quad , \tag{3.19}$$

the uncertainty of the function $\overline{f}(t)$ for small deviations $\Delta\tau$ of τ is given by

$$\Delta\overline{f}(t) = \left|\frac{\partial}{\partial\tau}\overline{f}(t)\right| \cdot \Delta\tau \quad , \tag{3.20}$$

where the derivative with respect to τ is

$$\begin{aligned}\frac{\partial}{\partial\tau}\overline{f}(t) &= \underbrace{\int\limits_{-\infty}^{t} \frac{t-t'}{\tau^3} e^{-(t-t')/\tau} f(t')\ \mathrm{d}t'}_{\frac{1}{\tau}\widetilde{f}(t)} - \underbrace{\int\limits_{-\infty}^{t} \frac{1}{\tau^2} e^{-(t-t')/\tau} f(t')\ \mathrm{d}t'}_{\frac{1}{\tau}\overline{f}(t)} \\ &= \frac{1}{\tau}\left(\widetilde{f}(t) - \overline{f}(t)\right) \quad .\end{aligned} \tag{3.21}$$

Setting $f(t) = p^{1-\frac{1}{\kappa}}(t)$, the absolute uncertainty can be written as

$$\Delta\overline{p^{1-\frac{1}{\kappa}}}(t) = \left|\frac{1}{\tau}\left(\widetilde{p^{1-\frac{1}{\kappa}}}(t) - \overline{p^{1-\frac{1}{\kappa}}}(t)\right)\right| \Delta\tau \quad . \tag{3.22}$$

Because our main interest lies in the error of the density, we use this result to calculate the relative uncertainty $\Delta\rho/|\rho|$ by inserting $\Delta\overline{p^{1-\frac{1}{\kappa}}}$ into Eq. 3.18 and dividing by $\rho(t)$. We arrive at a relation for the relative uncertainty of the density in dependence of the relative error in the time constant:

$$\boxed{\frac{\Delta\rho(t)}{|\rho(t)|} = \left|\frac{\widetilde{p^{1-\frac{1}{\kappa}}}(t)}{\overline{p^{1-\frac{1}{\kappa}}}(t)} - 1\right| \frac{\Delta\tau}{|\tau|} \quad . \tag{3.23}}$$

Notice that τ here is the actual, time dependent time constant of the temperature sensor. Since we are only interested in the order of the uncertainty we can, in a first approximation use the estimated time constant, which should be of the same order as the actual one.

Numerical Evaluation

In order to efficiently calculate the above described filters numerically, a recursive relation is preferable. Using a Taylor expansion of $\overline{f}$ and $\widetilde{f}$ in Eq. 3.21 and identifying the definitions in the expansion, will lead to the following recursion relations of third order accuracy [43]:

$$\overline{f}_n = \frac{\frac{2\tau}{\Delta t} e^{-\frac{\Delta t}{2\tau}} \overline{f}_{n-1} + f_n + f_{n-1}}{\frac{2\tau}{\Delta t} e^{\frac{\Delta t}{2\tau}}} + O\left(\left[\frac{\Delta t}{\tau}\right]^3\right) \tag{3.24}$$

$$\widetilde{f}_n = e^{\frac{-\Delta t}{\tau}} \widetilde{f}_{n-1} + \Delta t e^{\frac{-\Delta t}{\tau}} \overline{f}_{n-1} + \frac{\Delta t^2}{2\tau^2} f_n + O\left(\left[\frac{\Delta t}{\tau}\right]^3\right) \tag{3.25}$$

4. Methods

This chapter is a collection of all the calculation, computation and evaluation methods used for the later discussion of simulation and experimental results of pulsating flows in chapter 5.

4.1. Mass flow equation including unsteady friction and compressibility

In the following, the instantaneous, acceleration based unsteady friction model of Daily et al., discussed in section 2.3.2, will be applied in the derivation of a mass flow equation for unsteady orifice flow with fast density changes.

Starting point of the analysis is the momentum equation in its differential form, Eq. 2.8. The viscous and wall shear forces are approximated by the unsteady friction only, Eq. 2.18: $f_{viscous} + f_{wall} = -\rho k A \; \partial U / \partial t$, where k again is the unsteady friction coefficient.

Not including the steady friction, or pressure loss caused by it at this point will introduce an error which will be termed E_K in the following. Integrating the full momentum equation in axial direction $\int_{x_1}^{x_2} \mathrm{d}x$, over the distance L between the pressure tappings will result in

$$\int_{x_1}^{x_2} \frac{\partial}{\partial t}(\rho A U)\,\mathrm{d}x + \left[\beta_m \rho A U^2\right]_{x_1}^{x_2} = -\int_{x_1}^{x_2} A \frac{\partial p}{\partial x}\,\mathrm{d}x \qquad (4.1)$$

$$- k \int_{x_1}^{x_2} \rho A \frac{\partial U}{\partial t}\,\mathrm{d}x - E_K \quad .$$

Several assumptions or simplifications have to be made for the flow field, to be able to solve the above equation for the mass flow. Because the distance between the tappings is generally small in comparison with the wavelengths of pulsations arriving at the orifice, the density inside the measurement volume will be assumed constant. Yet, density is still considered time dependent, since large and rapid variations in pressure or temperature may occur in exhaust flows.

Two major simplification have to be made for the axial pressure gradient. For lack of information, the pressure has to be linearly approximated between the measurement tappings with constant gradient: $p(x,t) = p_1(t) + x\ \Delta p(t)/L$, where $x \in (x_1, x_2)$. In a corner tapping configuration, where both pressure tappings are placed adjacent to the orifice, this will produce small errors, but would significantly impact measurements with D - D/2 (tappings are placed one diameter upstream / half a diameter downstream of orifice) and flange (tappings are placed 25.4 mm upstream and downstream of orifice) tapping arrangements. This situation is illustrated in Fig. 4.1.

The second, more severe simplification was already made in the derivation of the momentum equation, when assuming a constant pressure over the cross section of the pipe. As will be shown later, this assumption is not justified and will lead to a significant error in the end. To bear this error in mind, an additional term E_p is introduced in the momentum equation.

The argument of a short measurement distance and the small variability therein, again is used for the unsteady friction term in Eq. 4.1. Local acceleration causing unsteady friction is being assumed constant: $\partial U(x,t)/\partial t \approx \partial U(x_1,t)/\partial t$ for $x \in (x_1, x_2)$. Carrying out the integration on the right hand side between the

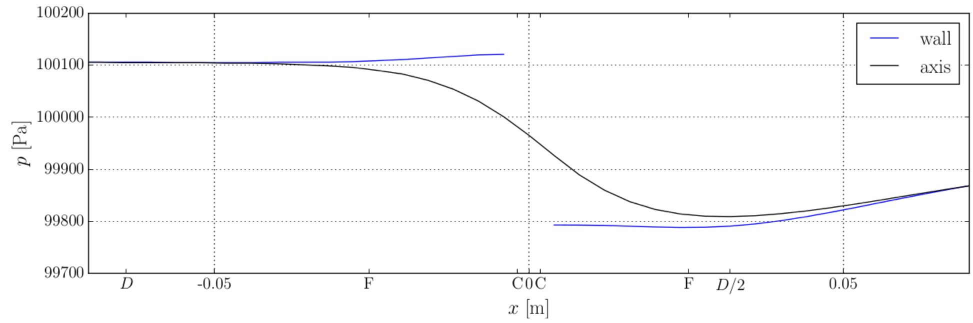

Figure 4.1.: Pressure over axial position x at centerline (axis) and wall of orifice meter with orifice plate located at $x = 0\ m$ in a 10 m/s mean, steady flow. Different tapping locations indicated by: C for corner tappings, D and $D/2$ for $D - D/2$ tappings and F for flange tappings.

equal control region boundaries $A_1 = A_2 = A$ with the above simplifications will yield:

$$\int_{x_1}^{x_2} \frac{\partial}{\partial t}\underbrace{(\rho A U)}_{J}\,\mathrm{d}x + [\beta_m \underbrace{\rho A U^2}_{J^2/(\rho A)}]_{x_1}^{x_2} = -\frac{V_0 \Delta p}{L} - \rho k V_0 \frac{\partial U_1}{\partial t} - E_K - E_p \quad . \tag{4.2}$$

For the remaining integral over the temporal change of the mass flow, a mean value of inlet temporal change $\frac{\partial J_1}{\partial t}$ and outlet temporal change $\frac{\partial J_2}{\partial t}$ is formed:

$$\int_{x_1}^{x_2} \frac{\partial J}{\partial t}\,\mathrm{d}x = \frac{L}{2}\left(\frac{\partial J_1}{\partial t} + \frac{\partial J_2}{\partial t}\right) \quad . \tag{4.3}$$

To identify the mass flow in the unsteady friction, the last term in Eq. 4.2 will be extended by ρA. Additionally, the time dependence of the density has to be considered when taking the time derivative:

$$
\begin{aligned}
&\frac{L}{2}\left(\frac{\partial J_1}{\partial t}+\frac{\partial J_2}{\partial t}\right)+\frac{\beta_{m,2}J_2^2}{\rho A}-\frac{\beta_{m,1}J_1^2}{\rho A} \\
&=-\frac{V_0\Delta p}{L}-\frac{kV_0}{A}\left(\frac{\partial}{\partial t}(\rho A U_1)-AU_1\frac{\partial \rho}{\partial t}\right)-E_K-E_p \quad .
\end{aligned}
\tag{4.4}
$$

With the definition of the mass flow this yields:

$$
\begin{aligned}
&\frac{L}{2}\left(\frac{\partial J_1}{\partial t}+\frac{\partial J_2}{\partial t}\right)+\frac{\beta_{m,2}J_2^2}{\rho A}-\frac{\beta_{m,1}J_1^2}{\rho A} \\
&\qquad=-\frac{V_0\Delta p}{L}-\frac{kV_0}{A}\left(\frac{\partial J_1}{\partial t}-\frac{J_1}{\rho}\frac{\partial \rho}{\partial t}\right)-E_K-E_p \quad .
\end{aligned}
\tag{4.5}
$$

This form still contains mass flows at both tappings of the control region, but J_2 can be eliminated with the use of the continuity equation, Eq. 2.5:

$$
\begin{aligned}
&L\frac{\partial J_1}{\partial t}-\frac{V_0 L}{2}\frac{\partial^2 \rho}{\partial t^2}+\frac{\beta_{m,2}}{\rho A}\left(J_1^2-2V_0 J_1\frac{\partial \rho}{\partial t}+V_0^2\frac{\partial \rho}{\partial t}^2\right)-\frac{\beta_{m,1}J_1^2}{\rho A} \\
&\qquad=-\frac{V_0\Delta p}{L}-\frac{kV_0}{A}\left(\frac{\partial J_1}{\partial t}-\frac{J_1}{\rho}\frac{\partial \rho}{\partial t}\right)-E_K-E_p \quad .
\end{aligned}
\tag{4.6}
$$

Finally gathering all terms of $\frac{\partial J_1}{\partial t}$, J_1^2 and J_1 will lead to the time derivative of the mass flow at the pressure tapping at x_1. To allow a better comparison with original flow meter equations, the term $(\beta_{m,1}-\beta_{m,2})J_1^2$ will be replaced by $(\beta_{m,in}-\beta_{m,out})\,\mathrm{sgn}(J_1)J_1^2$, where $\beta_{m,in}$ and $\beta_{m,out}$ are the momentum correction coefficients at the inlet and outlet boundaries,respectively, depending on flow direction.

$$\boxed{\begin{aligned}\frac{\partial J_1}{\partial t} = \frac{1}{L + \frac{kV_0}{A}} \Bigg\{ & \frac{1}{\rho A}(\beta_{m,in} - \beta_{m,out}) \operatorname{sgn}(J_1) J_1^2 \\ & + (2\beta_{m,2} + k) \frac{V_0}{\rho A} \frac{\partial \rho}{\partial t} J_1 - \frac{V_0^2 \beta_{m,2}}{\rho A} \frac{\partial \rho}{\partial t}^2 \\ & + \frac{L V_0}{2} \frac{\partial^2 \rho}{\partial t^2} - \frac{V_0}{L} \Delta p - E_K - E_p \Bigg\} \quad .\end{aligned}} \tag{4.7}$$

Simply setting $\frac{\partial J_1}{\partial t} = 0$ and $\frac{\partial \rho}{\partial t} = 0$ gives the steady, incompressible part of the mass flow equation:

$$0 = \frac{1}{\rho A}(\beta_{m,in} - \beta_{m,out}) \operatorname{sgn}(J_1) J_1^2 - \frac{V_0}{L} \Delta p - E_K - E_p \tag{4.8}$$

To evaluate the unsteady friction parameter, one may realign Eq. 4.7 to solve for k:

$$\begin{aligned} k = \frac{1}{\frac{V_0}{A}\frac{\partial J_1}{\partial t} - \frac{V_0}{\rho A}\frac{\partial \rho}{\partial t} J_1} \Bigg[& \frac{1}{\rho A}(\beta_{m,in} - \beta_{m,out}) \operatorname{sgn}(J_1) J_1^2 + \frac{2 V_0 \beta_{m,2}}{\rho A} \frac{\partial \rho}{\partial t} J_1 \\ & - \frac{V_0^2 \beta_{m,2}}{\rho A} \left(\frac{\partial \rho}{\partial t}\right)^2 + \frac{L V_0}{2} \frac{\partial^2 \rho}{\partial t^2} - L \frac{\partial J_1}{\partial t} - \frac{V_0}{L} \Delta p \\ & - E_K - E_p \Bigg] . \end{aligned} \tag{4.9}$$

Because we cannot asses the impact of steady friction E_K and cross sectional pressure distribution effects E_p, this is not solvable yet. For that reason further examination of the flow and pressure effects is needed.

4.1.1. Measured Pressure Difference

It is beneficial to have a closer look at the pressure difference measured between the two taps upstream and downstream of an orifice. The measured differential pressure $\Delta p_{measured}$ is in fact a sum of several interrelated effects and could be split into those major components contributing to the total pressure difference. Originally there is a static pressure gradient Δp_{static}, which causes a pressure-driven flow in a pipe in the first place. For steady flow, this gradient is needed to overcome the frictional losses at the orifice and maintain a steady flow. In unsteady flows, the static pressure gradient will be of time varying nature, common to (acoustic) waves or, generally speaking, pulsations.
Superimposed to the already described static pressure gradient is a differential pressure $\Delta p_{dynamic}$, which is the momentary, local pressure loss or increase described by the Bernoulli effect, caused by the convective acceleration through the orifice (Venturi effect).

An increase in the measured pressure difference has to be taken into account, if the pressure is measured in the vicinity of the orifice plate. There, one additionally measures a stagnation pressure at the upstream tapping: Because of the inertial forces, the outermost fluid particles are not able to follow the main fluid stream when it contracts through the orifice and thus will be slowed down at the orifice plate. Another way to view this increase in pressure, is the outward pressure increase linked with the inward curvature of the streamlines. Since at an ideal stagnation point dynamic pressure is fully converted to static pressure, a square like relation between flow speed and pressure increase could be expected.
On the downstream side, the sharp edge of the orifice plate forces the flow to separate, beginning at relatively low Reynolds numbers, causing a separation bubble, also called recirculation region, to form behind the plate. Fluid particles from the recirculation region, that are at the boundary to the main orifice jet, are entrained by faster vortices in the separated shear layer of the jet. This depletion creates the name giving recirculation and an accompanying lower pressure directly downstream of the orifice [44].

The pressure increase in front, and the decrease behind the orifice are mainly attributed to the form or geometry of the contraction and the location of the pressure tappings. For that reason, those two in this work are combined into one differential pressure termed impact pressure Δp_{impact}, with the name being coined by Mottram [1].

In sum the total, measured pressure difference can be written as:

$$\Delta p_{measured} = \Delta p_{static} + \Delta p_{dynamic} + \Delta p_{impact} \tag{4.10}$$

It has been already stated above, that the static pressure gradient acting on the orifice meter can be (and in combustion linked flows is) of unsteady nature. If a change in pressure occurs, the flow through the orifice will be accelerated/decelerated, trying to restore a stationary flow state. At very slow transients the fluid will be able to follow the varying pressure gradient in quasi-steady flow states, where the convectional forces on the left hand side of the momentum equation, Eq. 2.7, approximately balance out the pressure and frictional forces on the right side. As stated in the section about quasi-steady theory, section 2.5.1, local acceleration forces can only be neglected for low Strouhal number flows, i.e. flows at low frequencies. In most cases though, pressure changes occur much faster, not allowing the fluid to compensate for the change because of its inertia and viscous processes. This results in the before mentioned phase lag between the flow and the applied pressure gradient. Therefore the additional local acceleration has to be taken into account, which aims to correct present imbalances.

Based on the above considerations, we will further divide the static pressure gradient into two integral parts. The first part will be labeled $\Delta p_{effective}$ and describes the part of the pressure gradient that is *in phase* with the flux and is necessary to produce the momentary flux. For slow transients, $\Delta p_{effective}$ is approximately equal to the steady state static pressure gradient needed for the respective flow rate. In the case of faster transients it will considerably deviate from its steady state value, because of the pressure history dependent flow fields and associated momentum distributions.

The second part, which denotes the additional, *out of phase* pressure gradient, which stems from a fast pressure transient that is not yet compensated by the flow, is labeled $\Delta p_{transient}$. This superimposed pressure gradient locally accelerates the fluid. With this decomposition the resulting measured pressure difference becomes

$$\begin{aligned}\Delta p_{measured} = \Delta p_{effective} + \Delta p_{dynamic} + \Delta p_{impact} \\ + \Delta p_{transient} \quad .\end{aligned} \tag{4.11}$$

When calculating mass flow rates in practice, the measured pressure difference $\Delta p_{measured}$ is used for the pressure difference Δp in the equation for the temporal change of the mass flow, Eq. 4.7. Consequently, impact pressure, as well as steady frictional pressure losses are included in the calculation, but are usually neglected in the mass flow equation, i.e. $E_K = E_p = 0$.

Since the mass flow equation also has to hold for steady, incompressible flow, we can see from inserting the above pressure decomposition into the steady mass flow equation, Eq. 4.8, that including impact and friction pressure differences when neglecting E_K and E_p, will give an incorrect, higher calculated mass flux. For steady flows this usually is corrected by the calibration constant in the quadratic term, but may produce incorrect results, if the impact pressure and friction are not purely a function of J^2 .

For the full unsteady, compressible case the situation of course becomes more complicated, but valuable conclusions may be drawn nonetheless. Making use of the decomposition of the total measured differential pressure, Eq. 4.11, in the differential mass flow equation 4.7 gives:

$$\begin{aligned}\frac{\partial J_1}{\partial t} = \frac{1}{L + \frac{kV_0}{A}} \Bigg\{ & \frac{1}{\rho A}(\beta_{m,in} - \beta_{m,out}) \operatorname{sgn}(J_1) J_1^2 \\ & + (2\beta_{m,2} + k) \frac{V_0}{\rho A} \frac{\partial \rho}{\partial t} J_1 - \frac{V_0^2 \beta_{m,2}}{\rho A} \frac{\partial \rho}{\partial t}^2 \\ & + \frac{L V_0}{2} \frac{\partial^2 \rho}{\partial t^2} - \frac{V_0}{L} \Big[\Delta p_{effective} + \Delta p_{dynamic} \\ & + \Delta p_{impact} + \Delta p_{transient} \Big] - E_K - E_p \Bigg\} \quad .\end{aligned} \tag{4.12}$$

As said, effective-, dynamic- and impact-related pressure differences all are a consequence of the present, instantaneous flow field and do not cause a temporal change of the mass flow. Thus they can solely be attributed to the first term inside the curly brackets on the right hand side of Eq. 4.12 and the steady friction and pressure distribution errors, E_K and E_p. We can therefore identify

$$\boxed{\begin{aligned}& \frac{V_0}{L} \big(\Delta p_{effective} + \Delta p_{dynamic} + \Delta p_{impact} \big) \\ & \quad \overset{!}{=} \frac{1}{\rho A}(\beta_{m,in} - \beta_{m,out}) \operatorname{sgn}(J_1) J_1^2 - E_K - E_p \quad ,\end{aligned} \tag{4.13}}$$

where E_K and E_p represent all steady friction and impact pressure dependencies of the total pressure difference on the present, instantaneous flow field. Relation 4.13 is true for steady, as well as unsteady flows. Both sides together represent the quasi-steady part of the total differential mass flow equation.

The terms thus cancel out in the differential mass flow equation 4.12 and any change in mass flow for a given flux J with accompanying density and momentum distribution hence is the result of either a transient pressure $\Delta p_{transient}$ or a temporal change in density:

$$\frac{\partial J_1}{\partial t} = \frac{1}{L + \frac{kV_0}{A}} \left\{ (2\beta_{m,2} + k) \frac{V_0}{\rho A} \frac{\partial \rho}{\partial t} J_1 - \frac{V_0^2 \beta_{m,2}}{\rho A} \frac{\partial \rho}{\partial t}^2 \right. \\ \left. + \frac{L V_0}{2} \frac{\partial^2 \rho}{\partial t^2} - \frac{V_0}{L} \Delta p_{transient} \right\} \quad . \tag{4.14}$$

This allows to simplify the equation for the unsteady friction parameter k, Eq. 4.9, and leaves

$$k = \frac{1}{\frac{V_0}{A}\frac{\partial J_1}{\partial t} - \frac{V_0}{\rho A}\frac{\partial \rho}{\partial t} J_1} \left[\frac{2V_0 \beta_{m,2}}{\rho A} \frac{\partial \rho}{\partial t} J_1 - \frac{V_0^2 \beta_{m,2}}{\rho A} \left(\frac{\partial \rho}{\partial t} \right)^2 \right. \\ \left. + \frac{L V_0}{2} \frac{\partial^2 \rho}{\partial t^2} - L \frac{\partial J_1}{\partial t} - \frac{V_0}{L} \Delta p_{transient} \right] \quad . \tag{4.15}$$

At zero mean flow and momentum distributions not differing too widely from a uniform shape, the following relations, useful for the later analysis of transient measurements, have to hold:

$$\Delta p_{effective} + \Delta p_{dynamic} + \Delta p_{impact} \approx 0 \tag{4.16}$$

$$\Delta p_{measured} \approx \Delta p_{transient} \tag{4.17}$$

4.2. Flow Simulations in OpenFOAM

Proving the validity of the proposed methods for pulsating flows in an experimental setup obviously introduces a variety of unknowns to the measurements and does not allow an analysis of the flow mechanisms that produce the measured signals. Moreover, accurate devices for flow measurements in unsteady flows generally are scarce and usually expensive and no reference device that could correctly resolve the dynamic behavior of the flow or flux was available for the purpose of this work. To gain insight into the basic flow dynamics anyways, it was chosen to perform computational fluid dynamics simulations of the problem in *OpenFOAM* [45], a free, open source CFD software package that is licensed under the GNU General Public License. This would allow a more precisely defined environment for the evaluation of the discussed algorithms and their errors and would enable a more detailed analysis of the flow effects occurring at an orifice. However, care must be taken when comparing simulation results to real experiments and measurements, since the chosen turbulence model or any detail not included in the simulation models pose severe sources of error.

4.2.1. OpenFOAM Case Setup

A CAD model of the orifice meter in use for the experimental work was designed using *Gmsh* [46], a three-dimensional finite element mesh generator. Since any flow simulation of the full pipe geometry would have implied a considerable amount of computing time, it was decided to exploit the rotational symmetry of the problem and limit the simulation to a wedge geometry with an opening angle of $2°$. The model had a total length of 400 mm and a main pipe diameter of 63 mm. In the middle of the pipe a sharp orifice with an inner diameter of 45.9 mm and a thickness of 3.7 mm was placed. Directly adjacent to the orifice, the corner tappings were modeled with connecting ports of 1 mm width, extending to a diameter of 70 mm.

Again using *Gmsh*, a mesh of one cell thickness was created. The mesh was sectioned into three segments: one middle section for the closer vicinity of the orifice and two straight outer pipe sections. For the outer portions of the pipe, a radial distribution of 50 hexahedrons with a grading ratio of 1.02 to smaller cells towards the wall and an axial extension of 1 mm has been chosen. In the

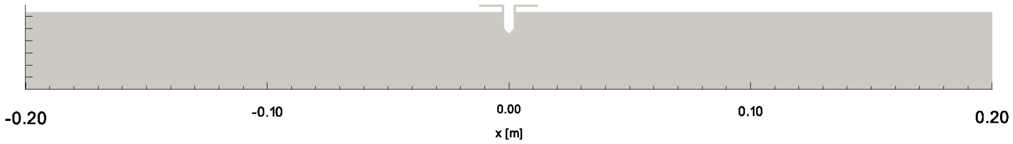

Figure 4.2.: Side view of wedge geometry used for simulations.

vicinity of the orifice plate a maximum edge length of 0.2 *mm* was set, to be able to resolve the expected turbulent processes in the surrounding of the orifice. As a result of the different mesh settings for the three segments, a majority of the cells in the middle section ended up non-orthogonal (see Fig. 4.3).

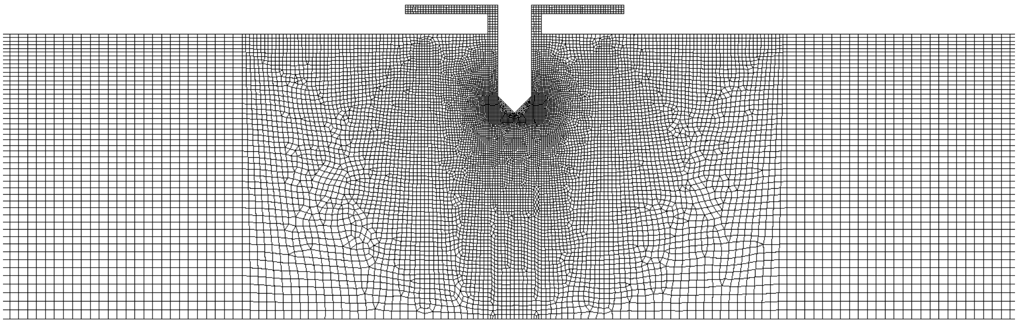

Figure 4.3.: Side view of the mesh in the vicinity of the orifice.

4.2.2. Steady Flow Simulations

The first goal in an attempt to validate the proposed models for unsteady flow measurement, was an assessment of the plausibility of the flow simulations for the case of steady air flow. To this end, several cases at different steady mass flow rates were set up. Each simulation was configured for compressible flow, using a standard k-ε turbulence model for Reynolds-averaged stress modeling. Thermophysical property modeling was realized applying the perfect gas model (*perfectGas*) for passive gas mixtures (*pureMixture*) and Sutherland's formula (*sutherland*) [47] for the calculation of the temperature-dependent transport properties.

Boundary Values and Initial Conditions

The flow field inside the orifice meter was initially set to zero velocity and uniformly distributed pressure of $10^5\ Pa$ and temperature of $293\ K$. μ_t, α_t, k and ε were calculated individually for each case, in accordance to the definitions given below, depending on the mean inlet velocity. For all cases an inlet turbulence intensity of 4% was used, which is reasonable for the Reynolds numbers in question [48]. The turbulent kinetic energy k and the turbulent dissipation rate ε were determined by

$$k = \frac{3}{2}(IU)^2 \tag{4.18}$$

$$\varepsilon = C_\mu^{3/4}\frac{k^{3/2}}{0.07D} \tag{4.19}$$

where the empirical constant $C_\mu = 0.09$. Turbulent viscosity μ_t then could be calculated by $\mu_t = \rho C_\mu k^2/\varepsilon$. Finally, the turbulent thermal diffusivity α_t is calculated from

$$\alpha_t = \frac{\mu_t}{Pr_t} \quad , \tag{4.20}$$

where a turbulent Prandtl number of 0.85 for air was used for all calculations.

At the upstream side of the geometry a mean inlet velocity U has been defined, for which a turbulent 1/7 power law velocity distribution was calculated. This was done by first calculating the maximal, center-line velocity $u_{max} = U(2n^2 + 3n + 1)/(2n^2)$, where the power law coefficient $n = 7$, and using this maximal velocity to calculate the turbulent velocity distribution from 2.11. For cases that fall in the laminar region, a laminar, parabolic profile has been used and turbulence parameters were set to zero. In total, eleven steady flow simulations were set up with mean inlet velocities of 0.05, 0.1, 0.5, 1, 2, 3, 4, 5, 10, 20 and 40 m/s. This corresponds to volume flow rates of about 10 to 7700 l/min. Table 4.1 gives an overview of the used boundary conditions for the flow variables at the wall, inlet and outlet. Patches on the front and back of the wedge geometry were assigned the *wedge* boundary condition for all variables to satisfy the axisymmetric condition of the problem.

Table 4.1.: Overview of boundary conditions for steady flow OpenFOAM simulations. Entries labeled '*calculated*' denote values calculated for each case in dependence of the mean flow velocity.

Variable	Wall	Inlet	Outlet
p	zero gradient	zero gradient	wave transmissive - 10^5 Pa
u	no slip	*calculated*	zero gradient
T	zero gradient	293 K	zero gradient
μ_t	μ_t-wall-function	*calculated*	zero gradient
α_t	α_t-wall-function	*calculated*	zero gradient
k	k-wall-function	*calculated*	zero gradient
ε	ε-wall-function	*calculated*	zero gradient

The needed boundary conditions for the turbulence parameters near the walls were modeled using the OpenFOAM implemented wall functions *mutkWallFunction*, *alphatWallFunction*, *kqRWallFunction*, *epsilonWallFunction* for μ_t, α_t, k and ε, respectively. . All cases were run on two processors, using the OpenFOAM *rhoPimpleFoam* solver for compressible, transient flow. Numerical schemes and used solver algorithms are printed in the OpenFOAM dictionaries *fvSchemes* and *fvSolution* in appendix A. For faster solution convergence of the steady flow simulations, the under-relaxation technique has been used, which limits the change of a flow field value from one iteration to the next by a multiplicative relaxation factor. Table 4.2 lists the used relaxation factors.

Table 4.2.: Relaxations factors f_R used in the steady flow simulations.

Variable	f_R
p	0.3
ρ	0.1
U, k, ε	0.7

Computation and Evaluation

All simulations were run until convergence was reached using a maximum CFL number of 0.95. When steady flow conditions were achieved, several samples were taken from the flow field. Flow rate measurements were taken at the inlet, outlet and at the upstream pressure tapping by integrating flow velocity times density over the cross section. The velocity profile at both tappings was used to calculate the momentum correction coefficient β_m. Additionally the pressure difference was evaluated at the pressure tappings and compared to the pressure difference acting at the axis.

4.2.3. Unsteady Flow Simulations

As a next step unsteady flow cases were set up, simulating pulsations, i.e. pressure waves, traveling from the inlet past the orifice towards the outlet.

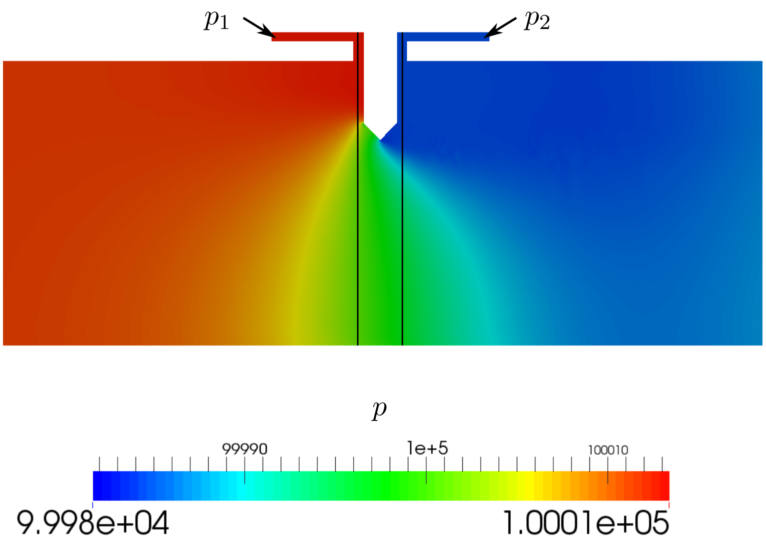

Figure 4.4.: Example pressure field for simulated steady flow from left to right (574 l/min). Black lines indicate sampling points for cross sectional flow field data and arrows indicate pressure sampling points for tapping pressure values.

Boundary Values and Initial Conditions

The initial conditions for the flow fields were the same as in the steady flow simulations. Three transient simulations have been run with various time-varying pressure signals at the inlet on the left and a pressure wave transmissive (i.e. non-reflecting) outlet on the right with a far field condition of a fixed pressure level in a distance of 2 m:

- Sinusoidal with a frequency of 30 Hz and amplitudes of 5000 Pa around 10^5 Pa; far field set to 10^5 Pa
- Sinusoidal with a frequency of 300 Hz and amplitudes of 3000 Pa around 103000 Pa; far field set to 98000 Pa
- Pressure in intake system of a two stroke engine running at 4000 rpm, simulated with *AVL BOOST*; far field set to 98000 Pa

Frequencies, amplitudes, offsets and far fields of the sinusoidal simulations were chosen this way because of the different flow effects being relevant for each case. The 30 Hz, 5000 Pa signal for example should lie at the boundary where Strouhal and Womersley numbers indicate, that inertial and viscous effects begin to play a role (compare section 2.3.2). In the 300 Hz simulation, inertial and viscous effects should play a dominant role and significant deviations in the flow profiles from well developed ones can be expected. The same inertia-, and viscosity-dominated behavior can already be observed at much lower frequencies, as was verified in simulations at 140 Hz in the course of this work. Nevertheless, the highest relevant frequency for combustion intake and exhaust flow was taken here, for illustration purposes.

The far field condition for the 300 Hz pulsation should produce a mean flow, without reverse mean flow occurring. In addition to the single frequency signals, the engine intake pressure waveform provides a practically relevant signal to test the performance of the proposed algorithms for a multi-frequency component signal.
Velocity boundaries have been set to the *OpenFOAM*-implemented *pressureInletOutletVelocity* boundary, which is a zero gradient condition for outflow and for inflow calculates the velocity from the flux inside the patch. Temperature, viscosity and turbulence boundaries have been set to *inletOutlet* boundaries, which are zero gradient conditions for outflow, but use predetermined or calculated boundary values for inflow. Table 4.3 gives a quick overview of the used boundary conditions for each flow variable.

Computation and Evaluation

The simulations were run using a maximum CFL number of 0.95, while sampling velocity, density and pressure distributions at the cross sections in front and behind the orifice plate as indicated in figure 4.4 at a rate of 10 kHz. Again flow rates and momentum correction coefficients were evaluated thereof and the pressure difference was determined at the pressure tappings.

Table 4.3.: Overview of boundary conditions for unsteady flow OpenFOAM simulations with transient, case dependent inlet pressure. Entries labeled '*calc.*' denote values calculated for each case and time in dependence of the mean flow velocity.

Variable	Wall	Inlet	Outlet
p	zero gradient	transient	wave transmissive
u	no slip	*inletOutlet*	*inletOutlet*
T	zero gradient	*inletOutlet* - 293 K	*inletOutlet* - 293 K
μ_t	μ_t-wall-function	*inletOutlet* - *calc.*	*inletOutlet* - *calc.*
α_t	α_t-wall-function	*inletOutlet* - *calc.*	*inletOutlet* - *calc.*
k	k-wall-function	*inletOutlet* - *calc.*	*inletOutlet* - *calc.*
ε	ε-wall-function	*inletOutlet* - *calc.*	*inletOutlet* - *calc.*

Based on the differential equation for the mass flux (Eq. 4.14), it is possible to calculate the mass flow rate from the density and its derivatives and the transient pressure $\Delta p_{transient}$, when both the unsteady friction k and the steady momentum correction coefficient $\beta_{m,2}$ are known. To actually solve the differential equation for the mass flow, Euler's method was used. The mass flow at time t_i is solely based on the mass flow and its time derivative at time t_{i-1}:

$$J_1(t_i) = J_1(t_{i-1}) + \frac{\partial J_1}{\partial t}(t_{i-1}) \cdot \Delta t \quad , \tag{4.21}$$

with the time step Δt . It should be noted here, that a higher order Runge-Kutta method would reduce the errors committed by the numerical scheme and should be used in future work. However this was not implemented in this work, since other sources of error were deemed far more significant at this stage.

Before any calculations could be run, the unsteady friction parameter k had to be determined. For this purpose, the sinusoidal pulsation simulations were used, because they provided a necessary, well defined environment. To determine k,

equation 4.15 was used, where the needed mass flow rate, density and respective derivatives where taken directly from the sampled data. Densities were averaged over the cross sections and all derivatives were calculated using second order accurate central differences. The momentum coefficient $\beta_{m,2}$ was determined using a piecewise cubic Hermite interpolating polynomial (PCHIP) to interpolate the values calculated from the steady flow simulations (Fig. 5.2).
The biggest challenge was the determination of the transient pressure $\Delta p_{transient}$, but it was possible to accurately calculate it with the help of the following two conditions:

- Acceleration at the orifice is caused by the gradient of the sinusoidal, traveling pressure wave that is coming from the inlet. The phase of this gradient or pressure difference between the two tappings can be calculated using the definition of a sinus wave traveling to the right - $p(x,t) = p_0 sin(2\pi f x/c - 2\pi f t + \varphi_0)$. Amplitude p_0, frequency f, speed of sound c and phase constant ϕ_0 are given by the initial and boundary conditions of the simulation.

- The incoming pressure wave will be partly reflected at the orifice, creating a higher pressure difference at the orifice. One can however calculate the amplitude of the transient pressure at zero mean flow, making use of the conditions previously stated for zero flow, equations 4.16 and 4.17. These say that at zero flow, the measured pressure difference has to approximately equal the transient pressure, since effective, dynamic and friction pressure differences are approximately zero.

For the calculation of the mass flow rate, $\Delta p_{transient}$ had to be determined without the use of information about the incoming pressure waves. According to equation 4.11, the transient pressure is the measured pressure difference minus the quasi-steady pressure differences:

$$\Delta p_{transient} = \Delta p_{measured} - \Big(\Delta p_{effective} + \Delta p_{dynamic} + \Delta p_{impact}\Big) \quad .$$

The quasi-steady pressure differences were approximated by applying relation 4.13 and using fourth order polynomial fits of the volume flow rate Q from the steady simulations for the right hand side:

$$\begin{aligned} &\frac{1}{\bar{\rho}}\big(\Delta p_{effective} + \Delta p_{dynamic} + \Delta p_{impact}\big) \\ &= A_1 Q + A_2 \operatorname{sgn}(Q) Q^2 + A_3 Q^3 + A_4 \operatorname{sgn}(Q) Q^4 \quad . \end{aligned}$$

Volume flow rates were used at this point, to eliminate density based mass flow differences. It should be mentioned, that Reynolds numbers should be used in future work since at constant volume flow rate, the pressure differences can still change because of the temperature dependence of viscosity. This should be expected in exhaust flow, were large temperature variations and different gas compositions are occurring.

To evaluate if this proposed procedure provides an enhancement on conventional temporal inertia theory, the mass flow rate has been calculated according to Mottram's differential mass flow equation, Eq. 2.39. The coefficient A was again determined using a quadratic regression of the steady flow simulation mass flow rates. Several different inertance coefficients B have been used in the evaluation. The specific values were taken as calculated by Doblhoff-Dier [34], since the same orifice metering device was used:

- $\mathbf{B} = \mathbf{0}$ [1/m]: Neglecting inertance at all, corresponds to the quasi-steady theory and should result in a inertial error effect for pulsatile flow rates.

- $\mathbf{B} = \mathbf{37.5}$ [1/m]: Calculated in accordance to ISO/TR 3313 [2] (Eq. 2.38) with an effective length of $L_\varepsilon = d$:

$$B = \frac{4}{\pi d C_C}, \quad \text{with} \quad C_C = \frac{1}{\beta_d^4 + \frac{\pi^2 d^4 A}{8}} \tag{4.22}$$

  were A is the regression parameter.

- $\mathbf{B} = \mathbf{52.5}$ [1/m]: As stated in [34], this value was used in earlier work done by AVL List.

- $\mathbf{B} = \mathbf{10.4}$, $\mathbf{B} = \mathbf{22.4}$ [1/m]: These smaller inertance values were used to represent smaller effective lengths L_ε, but their exact values had no deeper meaning.

Error determination

The different calculation models were evaluated based on two error quantities. Since the most important measure in mass flow metering is the deviation of the measured cumulative mass flow over a time span $t_2 - t_1$ from its true value, the *relative mass flow error* was the first parameter to determine the quality of the different models:

$$\text{relative mass flow error [\%]} = \frac{\int_{t_1}^{t_2} J \, \mathrm{d}t - \int_{t_1}^{t_2} J_{ref} \, \mathrm{d}t}{\int_{t_1}^{t_2} J_{ref} \, \mathrm{d}t} \quad . \tag{4.23}$$

This error definition is problematic in the case of zero true mean flow, where the denominator will be close to zero and relative errors would sky-rocket. Therefore the *absolute mass flow error* was used for simulations and experimental measurements with approximately zero mean flow, giving the rate of deviation from the true mean:

$$\text{absolute mass flow error [kg/s]} = \frac{\int_{t_1}^{t_2} J \ \mathrm{d}t - \int_{t_1}^{t_2} J_{ref} \ \mathrm{d}t}{t_2 - t_1} \quad . \tag{4.24}$$

Because mean values do not reveal any information about the dynamic behavior of a time dependent function, a second quantity was needed to characterize the different models. The (normalized) *root mean square error* (RMSE) is used as a measure of the dynamic behavior. It is the mean squared deviation of the calculated mass flow rates from the true rate, normalized by the peak-to-peak interval of the true rate:

$$RMSE \ [\%] = \frac{\sqrt{\frac{1}{N}\sum_{i=1}^{N}(J(t_i) - J_{ref}(t_i))^2}}{J_{ref,max} - J_{ref,min}} \quad . \tag{4.25}$$

4.3. Resonance Pipe Measurements

The ultimate aim of this work was an improvement of existing algorithms for mass flow measurement of unsteady, pulsating flows using an orifice meter without pulsation damping devices. For calibration purposes, to determine the unsteady friction parameter k for the orifice in use and test the proposed measurement algorithm in a pulsating environment, an experiment was set up. Since directly deploying the device in a complex environment like an engine intake or exhaust gas system would not have allowed for a well defined, controlled environment, it was chosen to use a resonance pipe, described in detail below, to create the desired pulsating flows. This however did not allow to reproduce the extreme pressure variations and temperature jumps common in engine exhaust systems.

4.3.1. General Measurement Setup

There were several requirements to be met by the experimental test rig. First of all, variable, steady mass flows of known flow rates were needed to calibrate the orifice meter for steady flows and gain an overall knowledge of the behavior of the device. Secondly, pulsations of well defined amplitude and shape, without any mean flow were necessary to gain insight in the unsteady measurement performance of the proposed algorithm. Furthermore, the ability to test the device in a pulsating environment with superimposed mean flow is necessary, as the only reliable criterion for the evaluation of occurring measurement errors was a comparison of the overall measured mean flow with the damped mean flow measured by a reference device.

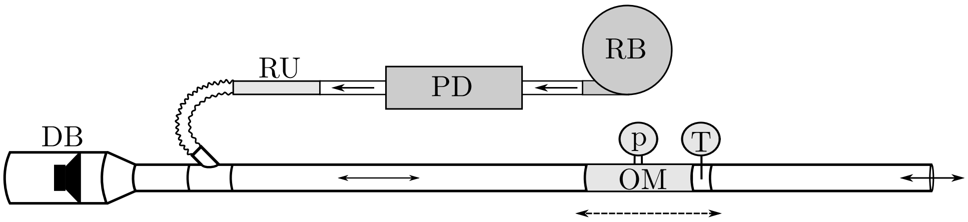

Figure 4.5.: Main resonance pipe setup with: (OM) movable orifice meter including pressure (p) and temperature (T) sensors, (DB) driver box including loudspeaker, (RU) reference unit, (PD) pulsation damper and (RB) radial blower.

To this end the test rig, schematically drawn in figure 4.5 , was set up. It consisted of six main elements: resonance pipe, acoustic driver box, orifice meter with temperature measurement, reference unit, pulsation damper and radial blower. The resonance pipe was assembled using smooth polypropylene pipe elements of 70 mm inner diameter and different lengths. In total the resonance pipe had a length of 6.45 ± 0.05 m, from the driver to the open end of the pipe. At the hereby defined upstream end of the pipe, the acoustic driver box containing the loudspeaker was attached. This was an aluminum cylinder of 255 mm diameter and 400 mm length, which had a conic section reducing to the resonance pipe's diameter within 200 mm at one end and was sealed at the other.

Inside the driver box, at a distance of 300 mm of the closed end, a loudspeaker with the same diameter was installed, resulting in the partition behind the speaker acting as an spring to the driver. Gaps between loudspeaker chassis and the enclosing pipe have been sealed with acoustic foam to prohibit any interference of phase shifted, reflected waves from the back end of the tube with the standing wave, but allowing for pressure equalization over time. The electric wiring of the speaker was routed out of the box through a small whole, which was sealed to prevent leakage. All signals applied to the driver were digitally generated using LabVIEW software.

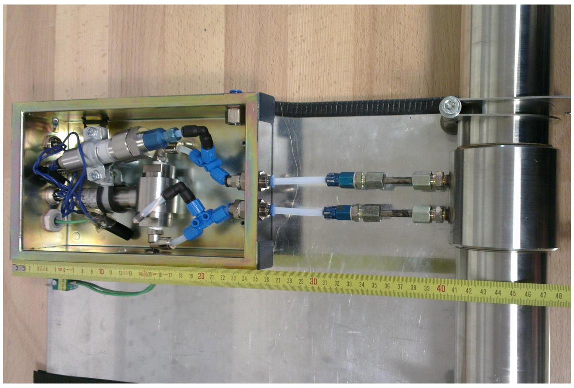

Figure 4.6.: Orifice meter, showing absolute and differential pressure transducer configuration. Length scale in centimeters.

With variable position along the resonance pipe, the orifice measurement system was installed. The orifice in use was taken from the AVL 442 Blow By Meter, which is commonly employed in steady flow rate measurements of calmed blow by gases in a range of 48 to 2400 l/min [49]. This 600 mm long pipe had an inner diameter of 63 mm and a 3.8 mm thick, sharp, symmetrical orifice plate of 45.9 mm diameter placed halfway through. Two tubes of 250 mm length connected the existing two corner tappings with a piezoresistive differential pressure transducer of type KELLER PD-23 with a measuring range of ± 100 $mbar$. At one tube, additionally a piezoresistive pressure transducer of type KELLER PAA-23 with a range of 0 to 2 bar for static pressure measurements was attached by a T-piece.

The opposing tube was compensated for the differing volume with a T-piece and a tube of same length (see Fig. 4.6).

In light of the above considerations for fast density determination, two K-type thermocouples of 0.5 and 1 *mm* diameter have been placed inside the orifice meter. They were fixed with a spacing of 1 *mm* between the measuring tips at the pipe center, using a thin wire running across the pipe cross section (Fig. 4.7). The pipe section containing the temperature sensors was then attached to the orifice pipe with a distance of about 300 *mm* to the orifice plate.

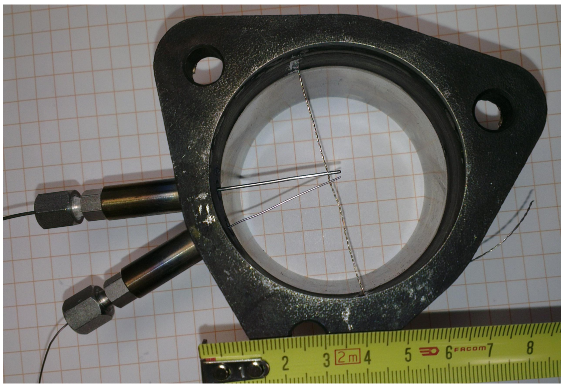

Figure 4.7.: Two thermocouple (0.5 and 1 *mm* ⌀) configuration for fast temperature measurement.

Pressure and temperature sensor signals have been digitally converted using *National Instruments* A/D converters. The signals of both pressure transducers were sampled at rates of $10kHz$, whereas the thermocouples were sampled at the highest possible rate of $100Hz$.

A Y-junction element in the resonance pipe with a reduced inner diameter of 30 *mm* of the branch pipe was positioned in front of the driver box. This side branch was used to create a steady mass flow inside the resonance pipe towards the open end, drawn in Fig. 4.5 on the right side. The steady flow was set using a PILLER radial blower with a maximum flow rate of 0.18 m^3/s or 10000 l/min. Due to the operating principle of the radial blower, inevitably generated pulsations which would influence any steady measurement had to be eliminated. For this reason a pulsation damper was installed preceding the reference unit in the direction of the flow. Employed damper and reference unit were an AVL 442 Blow By Meter system for steady flow measurements up to a maximum flow rate of 600 l/min. Drawbacks of the used flow meter were the low permissible flow rates on the one hand, and a high pressure loss caused by the pulsation damper on the other.

4.3.2. Setup Characterization

At first an evaluation of the measurement setup, the sensors and the resonance pipe at hand was necessary. This included an analysis of the measurement equipment signals for potential error sources, evaluation of the calibration coefficients for steady flow and a determination of the resonance modes of the resonance pipe.

Zero Flow Signals

The orifice meter was tested for its response in a quiescent setting to correct and adjust for measurement errors induced by the setup components. Main points of interest were the noise characteristics and the temporal drift of the differential pressure sensor, already described by Doblhoff-Dier [34] for the same equipment. After a system warm up phase of a few minutes and at no flow or other major acoustic excitation, the differential pressure signal was initialized to zero by averaging the sensor output voltage over a span of 5 seconds. Subsequently, the pressure signals were monitored over a few minutes to determine any occurring drift.

Pressure Transducer Analysis

Since measurement ranges and specified errors of the absolute and differential pressure transducers in use were different, it was unclear if the transducers had equal accuracy and temporal response in the frequency range of interest and if the absolute static pressure at the tapping side where no absolute pressure transducer was installed, could be approximated from the absolute pressure signal at the opposite side and the differential pressure signal.

Disconnecting the differential pressure transducer at the side opposite to the absolute pressure transducer and sealing the open ends of the disconnected tubes, made it possible to compare the pressure responses at the absolute pressure transducer side.

Steady Flow Calibration

For calibration purposes, the same setup as for the later conducted measurements with pulsations, but with a shorter resonance pipe length was used. The resonance pipe was shortened to reduce pressure losses and therefore allow for higher flow rates.

Pressure signals at the orifice were recorded for a few seconds for each flow rate set. Measurements were then repeated for the reversed orifice meter, to determine if differences in the pressure response existed for reverse flow. As stated above, only flow rates up to 600 l/min could be reached with the given setup.

Resonance Modes

To determine the resonance modes of the system, a white noise signal of constant spectral density was applied to the loudspeaker. The orifice meter was placed at the end of the resonance tube, resulting in a distance of 0.35 m between orifice plate and the open end. Static pressure amplitudes there should still be high enough for detection of the resonance modes.

Pressure signals at the orifice were then measured for a span of 30 s and a Fourier analysis was applied to determine the spectral components of the measured response.

The measured resonance modes were compared to numerically calculated resonances for a smooth pipe connected to a driver box with a conical transition, using a frictionless plane wave ansatz in the cylindrical pipes and a spherical wave ansatz in the conical section. Zero pressure amplitude boundary condition at the open end plus end correction and a mechanical, sinusoidal excitation at the driver side then were assumed to calculate the resonance frequencies according to Marx et al. [50].

4.3.3. Resonance Frequency Excitation

Knowing the resonance modes of the main pipe, it was the aim to use the driver to generate single frequency standing waves inside the pipe and use the well describable pressure and flow fields of standing waves to allow a measurement of the unsteady calibration parameter k. The orifice meter was first placed at positions of pressure antinodes. There, flow velocity should be zero for all times and therefore the differential pressure measured at the orifice should be small. The static pressure transducer would provide the pressure amplitude of the standing wave later needed to characterize the flow velocity at a pressure node. All measurements were run for 30 s after an initial offset correction.

Since the exact wave pattern at the driver end is heavily influenced by the shape of the driver box, all positions in the main pipe were referenced to the distance to the open pipe end, including an end correction of $0.85 \cdot r$. There a well defined pressure node and particle velocity antinode is present, which allows to better locate standing wave nodes inside the pipe.

The resonance pipe was excited at several different resonance frequencies, although the later detected influence of the resonance of the pressure measurement system at a frequency as low as 140 Hz invalidated most of the measurements at frequencies higher than 30 Hz. Therefore only two measurements are evaluated in this work. Th 139 Hz excitation case was the pointer in identifying the measurement resonances and the 30 Hz mode allowed an approximate assessment of the proposed procedure, which is why the evaluation of those two is explained in detail below.

139 Hz excitation

At an excitation frequency of 139 Hz ($11 \cdot \lambda/4$ - wave), the orifice meter was first positioned in the resonance tube with a distance of 0.60 ± 0.02 m between orifice plate and open end. This was the anticipated location of the first pressure antinode, taking into account the end correction of 0.0256 m.
Subsequently the orifice was moved to distances of 1.22 and 1.85 ± 0.02 m from the open end, where node and another antinode were assumed.

30 Hz excitation

For the excitation frequency of 30 Hz ($3 \cdot \lambda/4$ - wave), the orifice was positioned at a distance of 2.86 ± 0.02 m from the open end, what again was the location of the first pressure antinode. The orifice meter was then moved all the way to the open end of the pipe, resulting in a distance of 0.38 m between orifice plate and open end plus end correction. This was the only way to measure at a pressure node of the $3 \cdot \lambda/4$ - wave at the given total pipe length, since the driver box dimensions did not allow to place the orifice meter any closer to it.
At both locations, a spectral analysis of the absolute and differential pressure signals was done to identify the amplitudes of the 30 Hz components of the signals. With the static pressure amplitude, the maximum (cross sectional) mean flow velocity of the standing wave at a pressure node can be calculated using the impedance of the pipe, Eq. 2.41:

$$U = \frac{p}{\rho_0 c} \quad , \tag{4.26}$$

with the velocity of sound $c = \sqrt{\kappa \frac{p_0}{\rho_0}}$ and $\kappa = 1.4$ for air. To compare this mean flow velocity to the calculated velocity of the unsteady friction model, the measured signals were evaluated as follows.
Since, temperature stayed constant within the measurement uncertainty (± 0.2 K),

densities were determined using the measured temperature from the 0.5 mm thermocouple combined with the static pressure measured at the pipe, exploiting the adiabatic relation Eq. 3.18 given in the chapter about density calculation (chapter 3). The specified time constant of $\tau = 1.5 \pm 0.5s$ was used, where the uncertainty has been generously estimated in light of the considerations in chapter 3 for temperature measurement. The high uncertainty of the time constant however would not impact density calculations, due to the near constant mean pressure and temperature (see Eq. 3.18). Density derivatives were calculated using smooth noise robust differentiators of $19th$ order [51], although this again was of minor importance at this point, since obtained density variations were small for the given setup at 30 Hz.

5. Results and Discussion

5.1. Steady Flow Simulation in OpenFOAM

Although the main focus of this work was the unsteady flow measurement, it became apparent that a detailed analysis of the steady flow effects was necessary to reliably predict the unsteady behavior. In figures 5.1a and 5.1b velocity profiles, evaluated at the pressure tappings upstream and downstream of the orifice in the steady flow simulations are shown. The corresponding momentum correction coefficients are drawn in Fig. 5.2. These considerably deviate from unity, although this is traditionally assumed in orifice measurement theory. Main reason for this deviation is the higher weighting of the outer pipe sections due to their area, where the flow velocity is more severely affected by the orifice plate.

An asymptotic behavior towards $\beta_{m,1} = \beta_{m,in} = 1.90 \pm 0.01$ and $\beta_{m,2} = \beta_{m,out} = 2.54 \pm 0.01$ at higher flows can be observed for the momentum correction coefficients at the simulated flow speeds. At small flows larger changes in the coefficients are noticeable and no convergence towards definite values can bee seen. Since pressure measurement errors for flow rates $Q < 200\ l/min$ are already greater than the measurable pressure difference itself ($\Delta p \approx 3\ Pa$ in the simulation), the error induced by using the asymptotic β_m values for the whole measurement range in the calculation process is minimal. For this reason, the conventional steady flow meter equation in the form of $\Delta p = (A/\rho)J^2$, where A is a calibration constant, is providing satisfying results for carefully set up measurements.
Plotted in figure 5.3 is an exemplary radial static pressure distribution at a flow

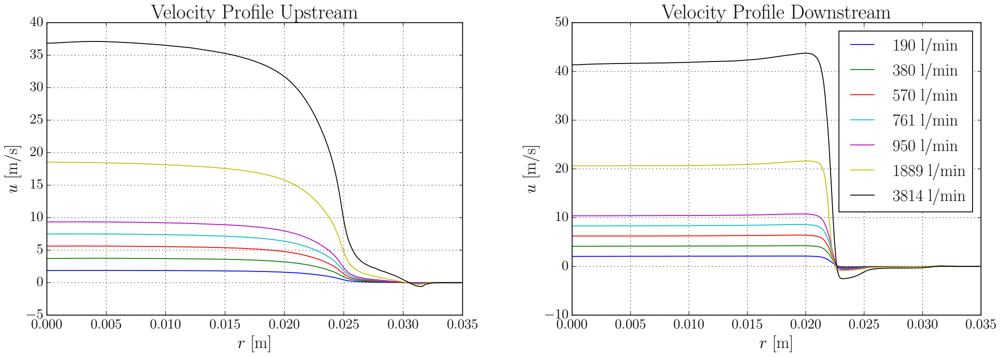

(a)

(b)

Figure 5.1.: Velocity profiles at the pressure tappings (a) upstream and (b) downstream of the orifice for steady flow at 1 to 20 m/s mean flow velocity.

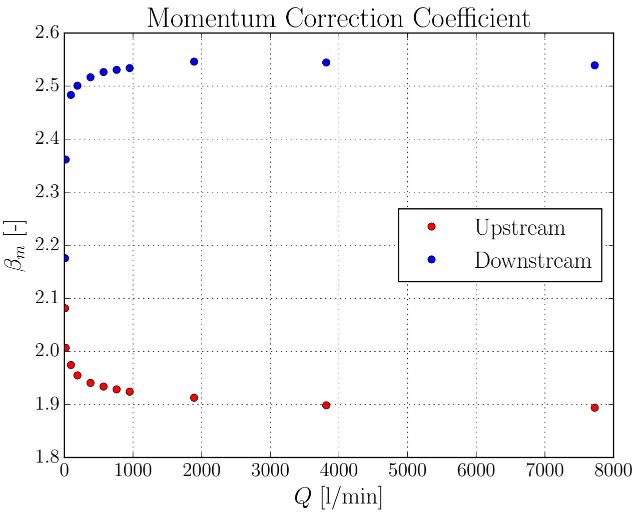

Figure 5.2.: Momentum correction coefficients for steady flow, calculated for the cross sectional velocity distributions at the upstream and downstream pressure tappings.

rate of 3814 l/min taken at the tappings, i.e. directly in front and behind the orifice plate. As is noticeable in Fig. 5.3, some irregularities, especially at the axis ($r = 0$), are visible in the pressure distributions. These irregularities are created by the used OpenFOAM solver when solving the pressure fields at highly non-orthogonal mesh cells, including the wedge shaped cells adjacent to the axis, and effected the pressure field inside those cells. Therefore centerline pressure values have a higher numerical uncertainty error.

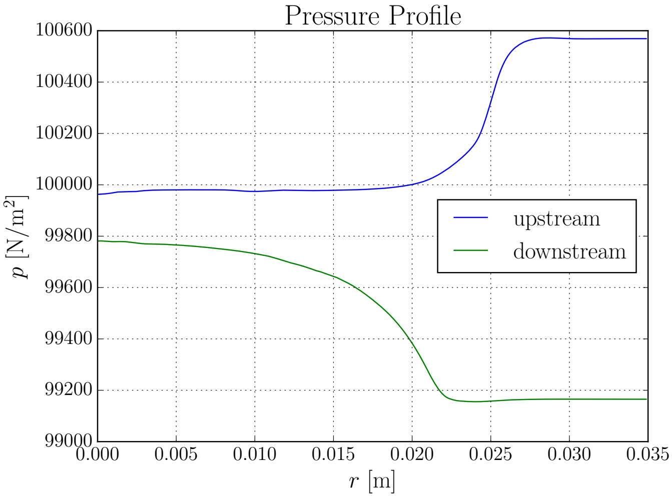

Figure 5.3.: Radial pressure distribution at the pressure tappings for steady flow at 20 m/s mean flow velocity, corresponding to 3814 l/min.

Beginning in the vicinity of the edge of the orifice ($r \geq 0.023\ m$), the upstream pressure shows a steep rise of about 600 Pa, caused by the stagnation at the orifice plate. This increase from the core pipe static pressure ($\approx 99970\ Pa$) is not considered in conventional flow meter equations for corner tapping configurations, although it amounts to almost half of the total measured pressure difference $\Delta p_{measured} = 1404\ Pa$. At the downstream side, a rather gradual drop away from the axis, up to the edge of the orifice can be observed ($r \leq 0.023\ m$). From there on, the downstream pressure stays almost constant. The gradual drop is caused by the velocity increase between the tappings and the associated Bernoulli effect,

which is considerably larger at the edge of the orifice (compare Figs. 5.6).In figures 5.4 and 5.5 the pressure differences between the pressure tappings (indicated in Fig. 4.4 by arrows) are marked by the red dots for the simulated steady cases. Centerline pressure differences are drawn in blue. All pressures have been divided by the cross sectionally averaged density to calculate the kinematic pressure, eliminating density- or temperature-based pressure variations and allowing for better comparison between measurements and simulations.
The large discrepancies between pressure differences at the tappings and the axis, are mainly a consequence of the impact pressure that is measured at the tappings in addition to effective and dynamic pressure drop. To underline the severity of the influence of the impact pressure, the steady flow equation 4.8 has been evaluated using mass flux and momentum correction coefficients from the CFD simulations to calculate the theoretical values of the sum of effective and dynamic pressure differences, $\Delta p_{eff.} + \Delta p_{dyn.}$. This pressure difference is also plotted in figures 5.4 and 5.5 and shows the large overestimation of the flow rate one would obtain in a corner tapping configuration, using an uncorrected or uncalibrated steady flow equation that simply attributes the measured pressure drop to an acceleration caused by the difference in (effective) cross sections at the tappings. At an ideal stagnation point, pressure velocity is zero and all kinetic energy, i.e. dynamic pressure, has been converted isentropically to static pressure. Since dynamic pressure in ideal flow is a function of the velocity squared and the stagnation pressure is the main part of the impact pressure, the near quadratic behavior of the total measured pressure difference $\Delta p_{measured} = \Delta p_{eff.} + \Delta p_{dyn.} + \Delta p_{impact}$ could be explained.

For the mentioned pressure differences, second order least squares fits with the fit function $\Delta p/\bar{\rho} = A\ \operatorname{sgn}(Q)Q^2$ have been carried out. These regressions were done only using the simulation measurement points up to 950 l/min. Fitting parameters A can be found in table 5.1. Comparing the fits in Fig. 5.5 to the simulations at flows higher than 950 l/min shows the higher order dependency of the measured, tappings pressure difference, that has to be considered. This

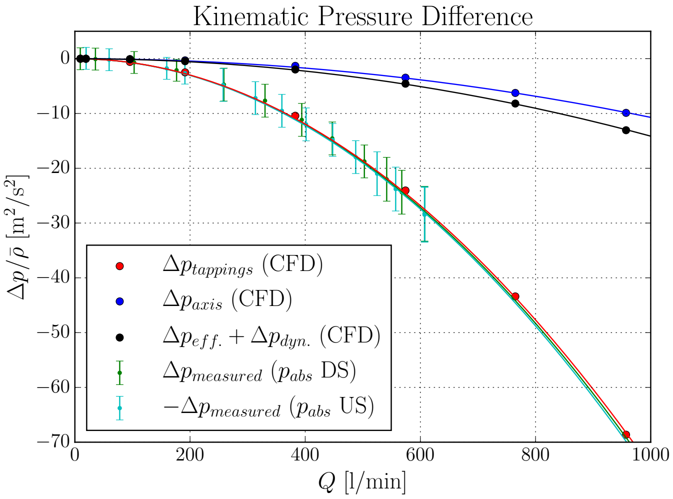

Figure 5.4.: Pressure differences measured in experiments and CFD simulations for small, steady flow rates. Solid lines are least squares fits, including only measurements and simulations up to 950 l/min.

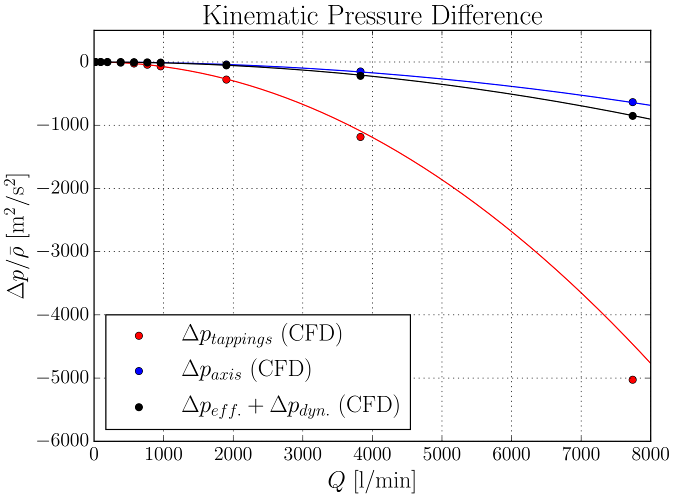

Figure 5.5.: Pressure differences measured in experiments and CFD simulations for steady flow up to 3814 l/min. Solid lines are least squares fits, including only measurements and simulations up to 950 l/min.

is also visible in the experimental calibration measurements, which have been plotted at this point for comparison purposes. Conventionally the additional non-linear behavior is empirically accounted for in the discharge coefficient in the Reader-Harris/Gallagher equation (Eq.2.33). The AVL 442 Blow By Meter uses a simple calibration polynomial of third order.

Due to the fact, that even the theoretical evaluation of $\Delta p_{eff.} + \Delta p_{dyn.}$ showed a noticeable higher order dependency for higher flow rates, both tappings pressure difference and the sum $\Delta p_{eff.} + \Delta p_{dyn.}$ were fitted with the fourth order polynomials $\Delta p/\bar{\rho} = A_1 Q + A_2 \,\mathrm{sgn}(Q) Q^2 + A_3 Q^3 + A_4 \,\mathrm{sgn}(Q) Q^4$ for later use in the calculations for unsteady flow. Regression parameters thereof can be found in table 5.2.

Table 5.1.: Parameters A in least squares fits for pressure differences $\Delta p/\bar{\rho} = AQ^2$ in steady flow simulations, only using flow rates up to 950 l/min.

Δp	A [m^{-4}]
$\Delta p_{tappings}$	-268194
Δp_{axis}	-38562
$\Delta p_{eff.} + \Delta p_{dyn.}$	-50896

Table 5.2.: Fit parameters in least squares fit for pressure differences $\Delta p/\bar{\rho} = A_1 Q + A_2 \,\mathrm{sgn}(Q) Q^2 + A_3 Q^3 + A_4 \,\mathrm{sgn}(Q) Q^4$ in steady flow simulations.

Δp	A_1 [m^{-1}s^{-1}]	A_2 [m^{-4}]	A_3 [sm^{-7}]	A_4 [s^{2}m^{-10}]
$\Delta p_{tappings}$	3.16829678	-258271.004	-692549.438	2739966.4
$\Delta p_{eff.} + \Delta p_{dyn.}$	43.377324	-53677.891	-43713.9393	466231.669

5.2. Unsteady Flow Simulations in OpenFOAM

5.2.1. 30 Hz Pulsation

As mentioned before, the low frequency case should give good results even using the quasi-steady approach, since inertia effects should still be low. Figures 5.6a and 5.6a show the instantaneous velocity distributions plotted at quarters of the full pulsation cycle. The velocity profiles are still in close agreement with the steady ones and the momentum correction coefficients, drawn in Fig. 5.7, for most of the time are close to the asymptotic steady values, which will be used in the calculations later on. Only at the points in time where mean flow goes to zero, β_m becomes ill defined, because it is inversely proportional to the mean flow. At the flow direction dependent inlet side, the momentum correction coefficient is mostly below the asymptotic value $\beta_{m,in}$. This increases the difference $(\beta_{m,in} - \beta_{m,out})$ compared to the quasi-steady approximation and will lead to an overestimation of the flow rate. At maximum flow rate for example, the difference is increased by approximately 11 %, leading to an equivalent mass flow rate error (see Fig. 5.11).

First the unsteady friction parameter was determined. k is plotted in dependence of the instantaneous acceleration/deceleration in figure 5.8. The large fluctuations around zero acceleration are caused by the vanishing denominator in k. It is distinguished between accelerating and decelerating flows, to examine if differences in the unsteady friction parameter for acceleration and deceleration can be found, as suggested by unsteady pipe flow theory.
Disregarding friction values of accelerations/decelerations near zero, showed that $k = 5.4 \pm 0.5$ for acceleration and deceleration. Because of the high uncertainty, no difference between acceleration and deceleration friction values could be determined. A fixed unsteady friction $k = 5.4$ was therefore used in the calculation of the mass flow. Since this value was later confirmed for all unsteady simulation cases, it was the one retained for all following mass flow calculations using the unsteady friction model.

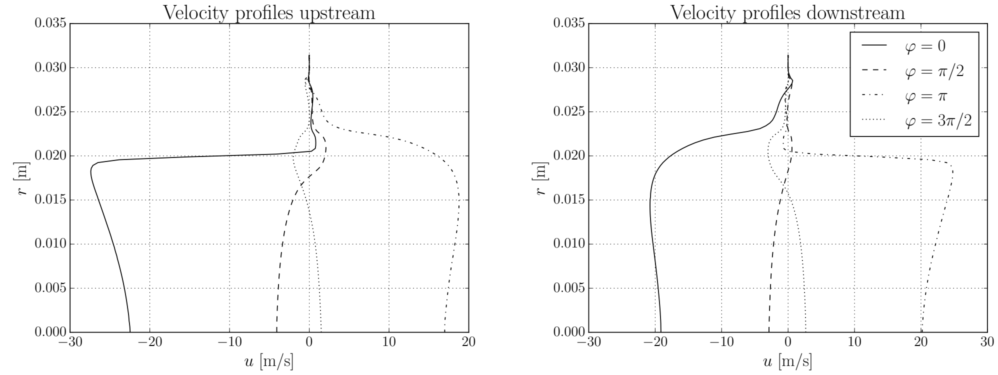

(a) (b)

Figure 5.6.: Velocity profiles at the pressure tappings (a) upstream and (b) downstream of the orifice for the 30 Hz pulsation simulation. φ is the phase in the transient pressure difference cycle, starting at zero pressure difference (i.e. maximum flow rate). The phase angles of $\varphi = 0,\ \pi/2,\ \pi,\ 3\pi/2$ correspond to times $t = 0.0589,\ 0.0672,\ 0.0756$ and $0.0839\ s$, respectively.

Figure 5.9 shows the measured pressure difference between the tappings for the 30 Hz simulation. The solid lines represent the quasi-steady and transient pressure differences calculated with the proposed unsteady friction model. For comparison purposes, the pressure differences which are calculated from the boundary conditions of the CFD simulations with the traveling wave ansatz, according to page 61, are drawn in dashed lines.

One can see that the phase difference between the applied transient pressure difference and the momentary flow, i.e. $\Delta p_{q.s.}$, produces an asymmetric total, measured pressure difference even though the mass flow is sine-shaped. This behavior validates the assumption of the measured pressure difference being a superposition of a quasi-steady and a transient part. There is another interesting feature at the point of flow reversal: The quasi-steady pressure difference is forced to go through zero with the assumed polynomial behavior, whereas the real pressure difference does not exhibit this behavior. This causes a local underestimation of $\Delta p_{q.s.}$, which results in an overestimation of the transient pressure difference $\Delta p_{trans.}$ and the calculated change of the mass flow rate (compare Fig. 5.10, e.g. at $t \approx 0.036\ s$), ultimately leading to an additional overestimation of the flow

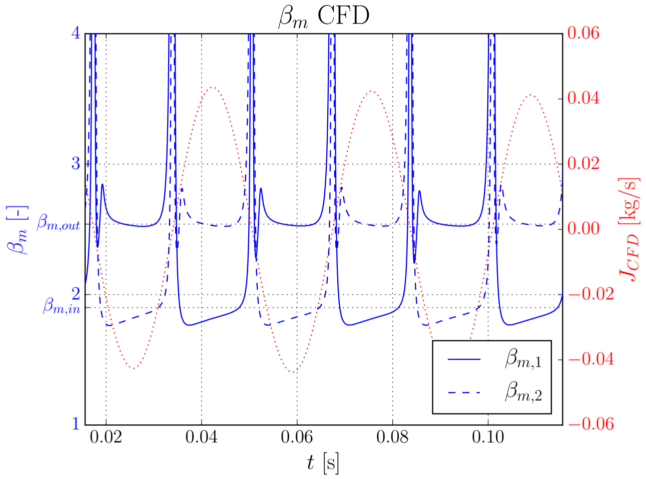

Figure 5.7.: Actual momentum correction coefficients β_m for 30 Hz pulsation simulation. Steady flow, asymptotic values for inlet and outlet momentum correction coefficients $\beta_{m,in} = 1.90$ and $\beta_{m,out} = 2.54$ are marked on y-axis.

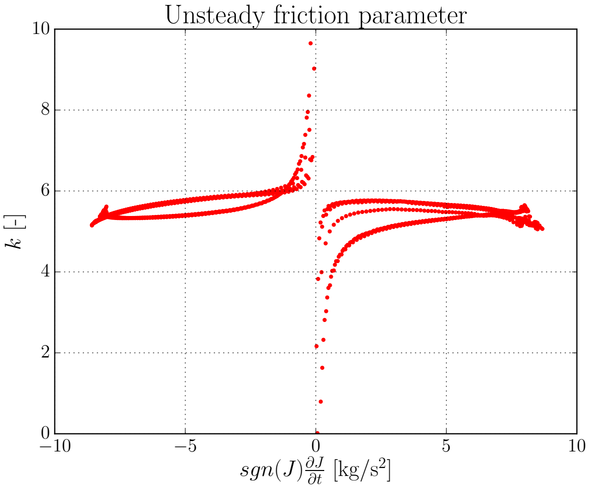

Figure 5.8.: Unsteady friction parameters k for each point in time in the 30 Hz pulsation simulation, plotted against instantaneous acceleration/deceleration.

rate.

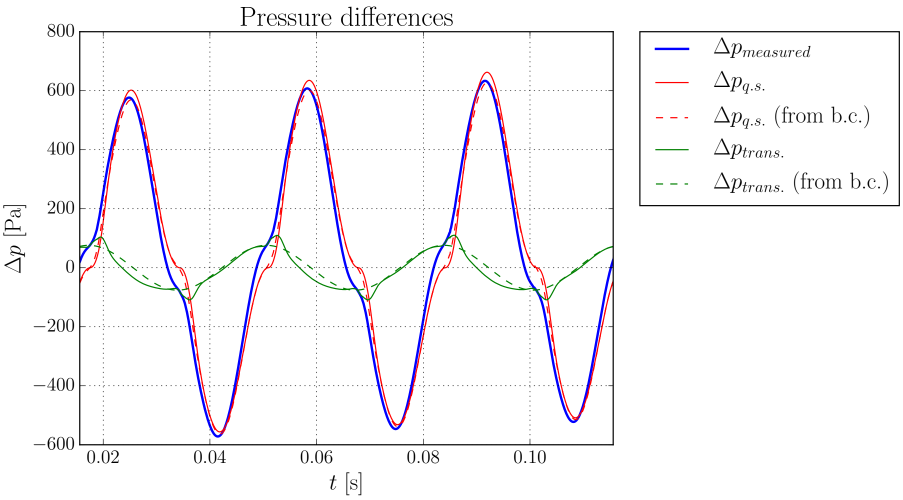

Figure 5.9.: Measured pressure difference $\Delta p_{measured}$ in the 30 Hz pulsation simulation. Unsteady friction model calculated quasi-steady and transient pressure difference fractions, $\Delta p_{q.s.}$ and $\Delta p_{trans.}$. Pressure differences denoted "from b.c.", are the calculated values from the boundary conditions of the simulation.

The actual and calculated mass flow rates, as well as the respective mass flow rate errors and root mean square errors are plotted in figures 5.11 and 5.12. As expected, neither model or change in inertance B (as specified on page 62) seems to cause a drastic deviation from the real flow rate. Though, RMS errors show that the unsteady friction model and an inertance value of $B \approx 10$ are best capturing the dynamic behavior of the flow. Higher inertance values exhibit a phase lag behavior in the calculated mass flow rate.

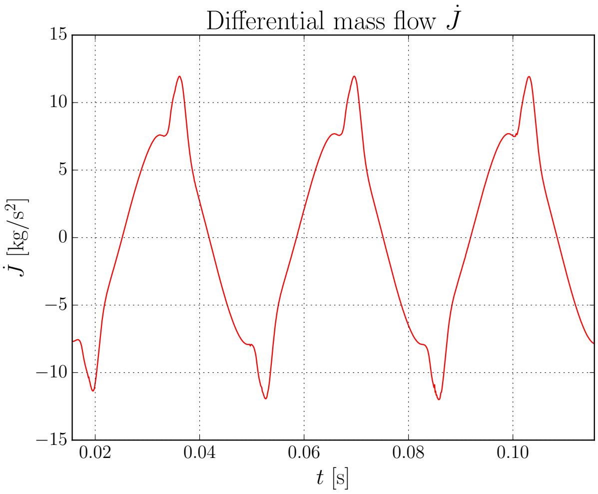

Figure 5.10.: Time rate of change of the mass flow rate for the 30 Hz pulsation case, calculated with the unsteady friction model.

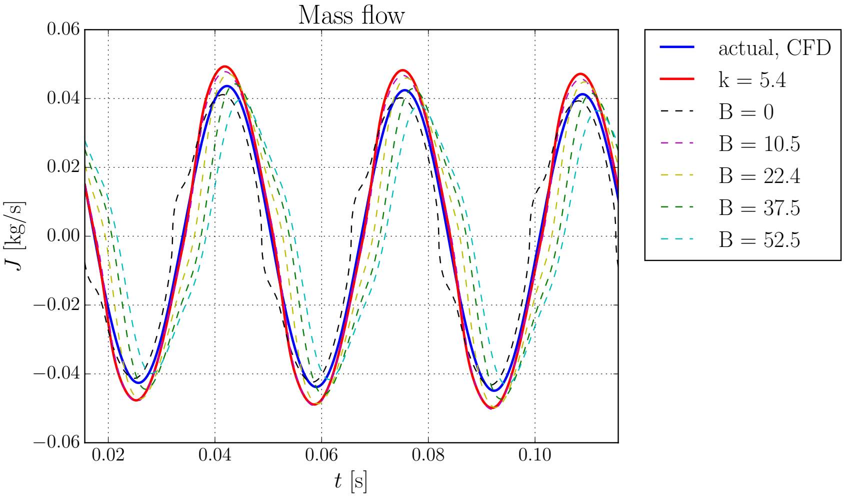

Figure 5.11.: Actual and calculated mass flow rates for the 30 Hz pulsation case, using the unsteady friction model and the classical inertia model with different values of B, as specified on page 62.

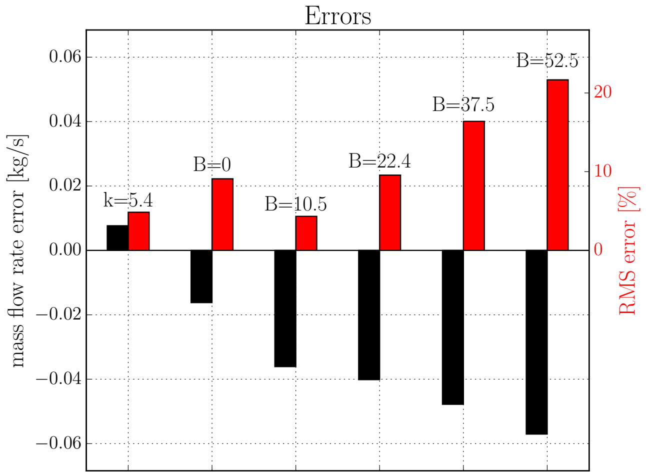

Figure 5.12.: Absolute mass flow errors and root mean square errors (RMSE) for the unsteady friction model and the classical inertia model with B as specified on page 62, in the case of a 30 Hz pulsation.

5.2.2. 300 Hz Pulsation

At a pulsation rate of 300 Hz inertial effects should already play a dominant role. Velocity distributions and corresponding momentum correction coefficients of the 300 Hz simulation are plotted in figures 5.13 and 5.14. The momentum coefficients again start to deviate strongly from the steady behavior when the mass flow approaches zero. In the velocity distributions one can see, that locally reverse flow occurs at the tappings even though mean flow is positive at all times.

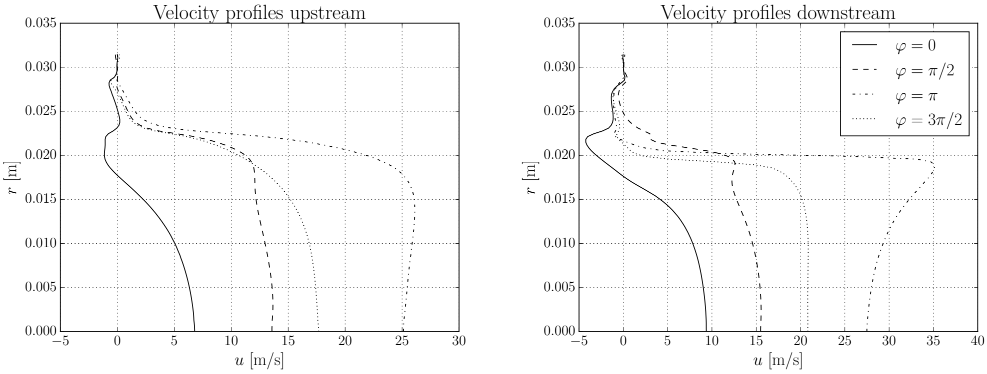

(a)

(b)

Figure 5.13.: Velocity profiles at the pressure tappings (a) upstream and (b) downstream of the orifice for the 300 Hz pulsation simulation. φ is the phase in the transient pressure difference cycle, starting at zero pressure difference (i.e. maximum flow rate). The phase angles of $\varphi = 0,\ \pi/2,\ \pi,\ 3\pi/2$ correspond to times $t = 0.0197,\ 0.0205,\ 0.0214$ and 0.0222 s, respectively.

Evaluation of the unsteady friction revealed a slightly different pattern, than the one at 30 Hz (Fig. 5.15). However, this can be attributed to the temporal uncertainty of the calculated phase of the incoming traveling wave, as described on page 61. It also explains a small difference observed between acceleration and deceleration friction values and thus did not allow a distinction between those two. Therefore, again only one unsteady friction parameter, $k = 5.4 \pm 0.5$, could be determined for acceleration and deceleration.

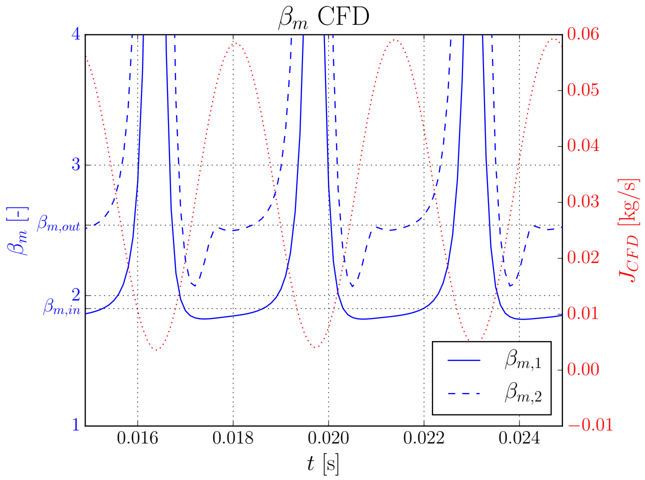

Figure 5.14.: Actual momentum correction coefficients β_m for 300 Hz pulsation simulation. Steady flow, asymptotic values for inlet and outlet momentum correction coefficients $\beta_{m,in} = 1.90$ and $\beta_{m,out} = 2.54$ are marked on y-axis.

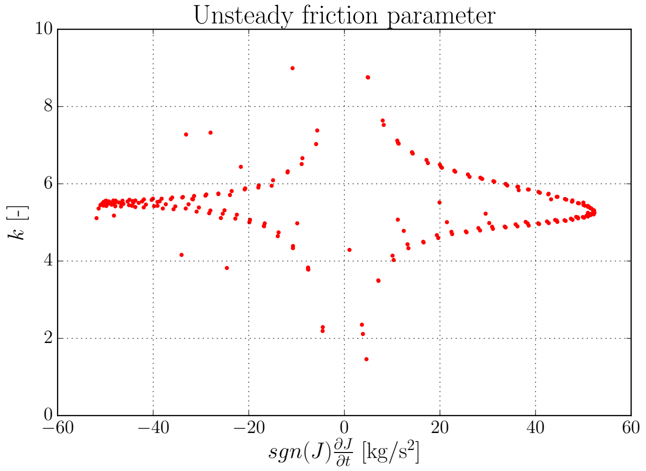

Figure 5.15.: Unsteady friction parameters k in the 300 Hz pulsation simulation, plotted against instantaneous acceleration/deceleration.

Quasi-steady and transient pressure differences calculated with the unsteady friction model (see Fig. 5.16), are in good agreement with the ones inferred from the boundary conditions. Nevertheless the eventually calculated mass flow rate is overestimating the true value. This can be seen for all calculations including the inertance of the orifice. Corresponding errors in figure 5.18 show, that the overestimation of the mean flow rises with increasing inertance B. Since assuming an inertia that is too high has an averaging effect, the square root error as mentioned in section 2.5.1 will lead to the observed overestimation of the flow rate.

As was the case in the 30 Hz simulations, the unsteady friction model and the conventional inertia model with a value of $B \approx 10$ produce similar results since terms including the density derivatives are small in comparison to the transient pressure difference term in the unsteady friction model. Both calculations produced relative errors of around 10 % and exhibited the best dynamic behavior.

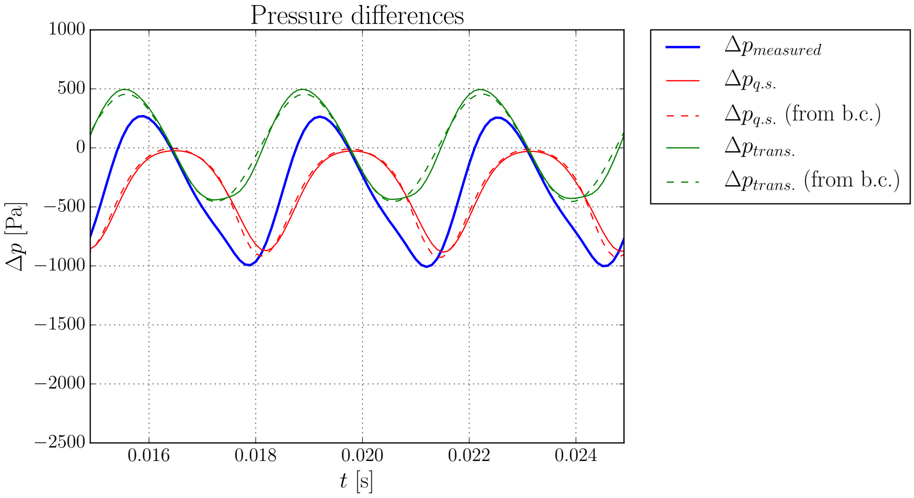

Figure 5.16.: Measured pressure difference $\Delta p_{measured}$ in the 300 Hz pulsation simulation. Unsteady friction model calculated quasi-steady and transient pressure difference fractions, $\Delta p_{q.s.}$ and $\Delta p_{trans.}$. Pressure differences denoted “from b.c.”, are the calculated values from the boundary conditions of the simulation.

The quasi-steady calculation with $B = 0$ clearly illustrates the inertial error, as described in section 2.5.1, showing an overestimation during acceleration phases and an underestimation of the flow rate during deceleration phases. It additionally results in a drastic underestimation of the total flow rate in this case, because a positive pressure difference is measured in deceleration phases and directly assigned to a negative flow rate.

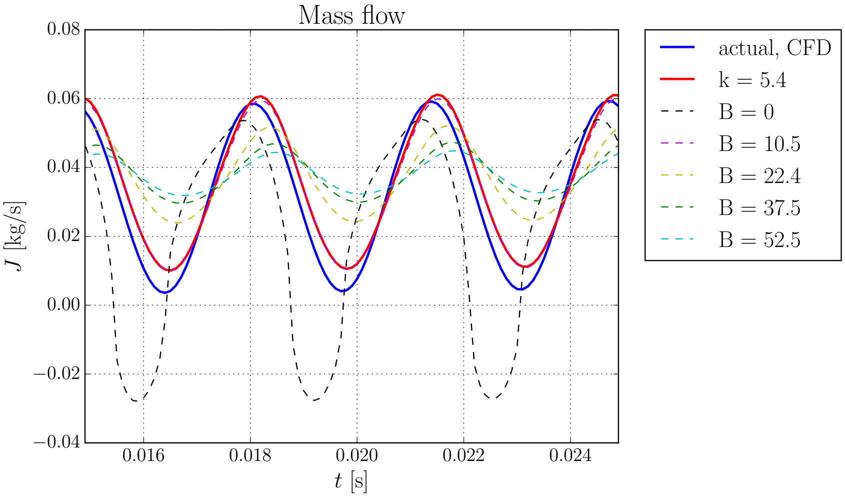

Figure 5.17.: Actual and calculated mass flow rates for the 300 Hz pulsation case, using the unsteady friction model and the classical inertia model with different values of B.

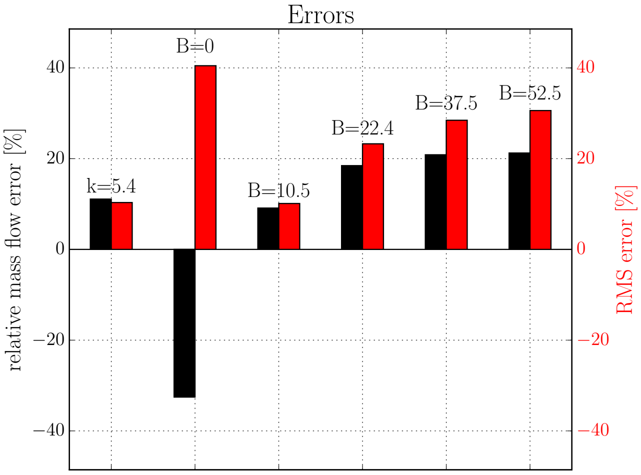

Figure 5.18.: Relative mass flow errors and root mean square errors (RMSE) for the unsteady friction model and the classical inertia model with different values of B in the case of a 300 Hz pulsation.

5.2.3. Engine Intake

Both simulations discussed above were special cases involving either no mean flow (30 Hz simulation) or a pulsation frequency on the boundary of the practical relevance (300 Hz simulation). They are important for the understanding of the underlying flow physics, but do not allow to estimate the errors made in practical situations. Results of the intake flows of a two cylinder engine running at 4000 rpm are presented in figures 5.20 and 5.21.

Because the pulsation amplitude is noticeably smaller than the mean flow most of the time and therefore flow distribution stays in a quasi-steady state, the momentum correction coefficients plotted in Fig. 5.19 are close to the asymptotic steady inlet and outlet values. Only when flow is heavily decelerated to almost zero mean flow at $t = 0.027\ s$, considerable momentum distribution deviations occur.

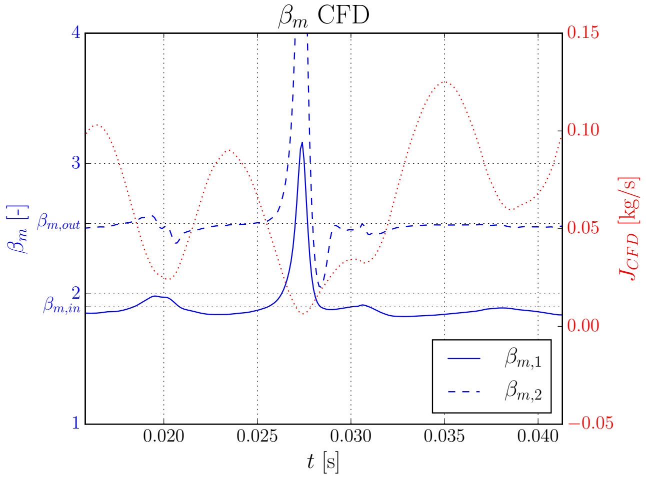

Figure 5.19.: Actual momentum correction coefficients β_m in the simulations of the intake of a two cylinder engine running at 4000 rpm. Steady flow, asymptotic values for inlet and outlet momentum correction coefficients $\beta_{m,in} = 1.90$ and $\beta_{m,out} = 2.54$ are marked on y-axis.

Again, the unsteady friction model and the conventional inertia model with a value of $B \approx 10$ deliver the lowest errors, although both models fail to capture the real flow behavior when the flow rate comes close to zero. Higher inertial coefficients again show a rising averaging behavior, resulting in a rising overestimation of the total mean flow.

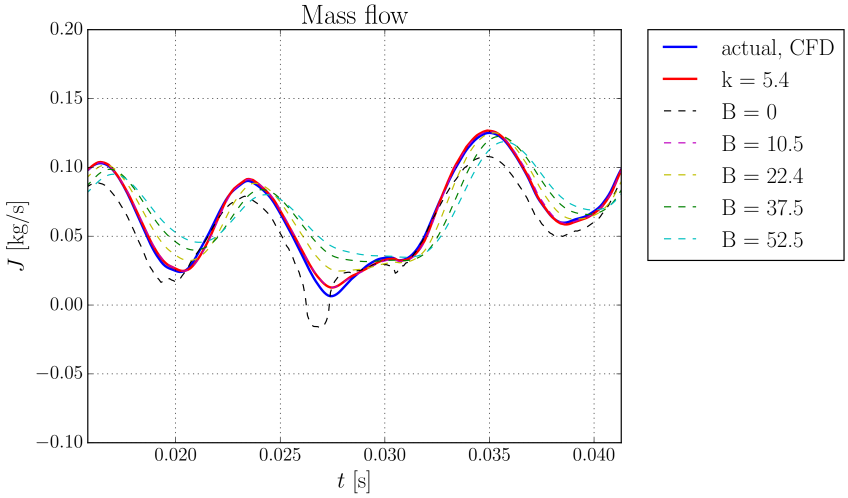

Figure 5.20.: Actual and calculated mass flow rates for the intake of a two cylinder engine running at 4000 rpm, using the unsteady friction model and the classical inertia model with different values of B.

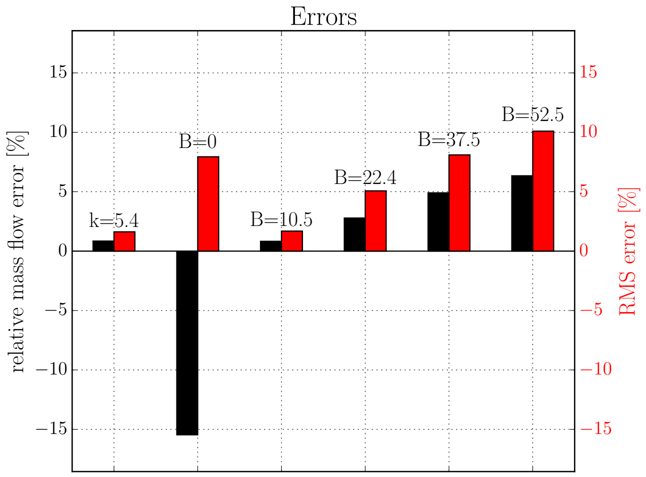

Figure 5.21.: Relative mass flow errors and root mean square errors (RMSE) for the unsteady friction model and the classical inertia model with different values of B simulated for the intake of a two cylinder engine running at 4000 rpm.

5.3. Resonance Pipe Measurements

5.3.1. Setup Characterization

Zero Flow Signals

Power spectral densities of absolute and differential pressure signals recorded for six minutes at no flow or deliberate acoustic excitation are plotted in figure 5.22. The spectra were calculated using Welch's methed, computing the average spectrum of 1 second, 50 % overlapping and Hanning-windowed time-segments. Clearly electronic noise can be identified at frequencies above 1000 Hz. However, there also were significant spectral components around 140 Hz present in the measured differential pressure signal. The frequency was later identified as a resonance frequency of the resonance pipe and of the pressure measurement system. Since at the time of measurement the orifice meter was fully assembled and installed in the resonance pipe, it remained unclear if this peak is a result of the electronic setup, including the transducers, or a consequence of unwanted exterior excitation causing repeated resonances in the resonance tube or the pressure measurement system.

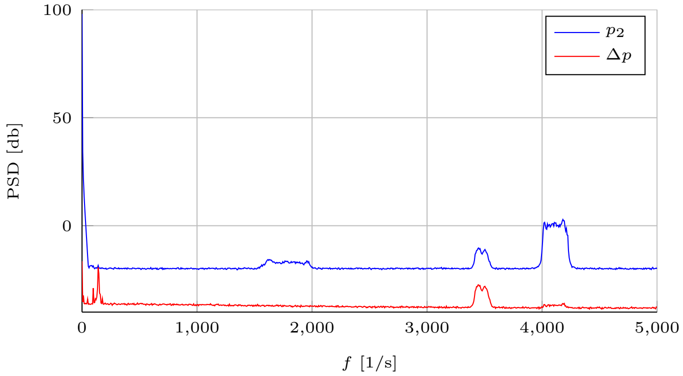

Figure 5.22.: Power spectral densities of measured absolute and differential pressures with no flow or acoustic excitation over a span of 6 min, calculated with Welch's method.

The differential pressure signal showed a noise root mean square value of 2 Pa and a drift of 0.2 Pa over the 6 minute span. Static pressure measurement relative noise root mean square was 20 Pa. Because the noise peak-to-peak levels in the differential pressure signal were low in comparison to the expected pressures differences and in the case of the present high frequency noise only the mean will effectively cause a flow, it was decided not to digitally filter the pressure signals. One second, moving averages over the differential pressure showed a quick rise of the offset up to 0.1 Pa in the first 10 seconds, even though the offset was corrected before the start of the measurement. Since a mean differential pressure of 0.1 Pa is already attributed to flow rates of about 40 l/min with the orifice and pipe diameters in use, this results in substantial error rates. As a consequence, dynamic flow rate measurements should be confined to short time spans and offsets should be corrected in between to keep errors low.

Pressure Transducer Analysis

Two example response comparisons of the absolute pressure transducer and the converted differential pressure transducer are shown in figures 5.23 and 5.24. At frequencies below approximately 100 Hz and amplitudes of 1000 Pa the signals were still in good agreement, but were diverging above the given thresholds. It is unclear which transducer is providing more reliable values, but because of the high specified uncertainty of the absolute pressure transducer ($\pm 500\ Pa$) and because of the sinusoidal response (which was the supplied loudspeaker signal) of the differential pressure transducer, the latter one should be more trustworthy. For the stated reasons, simple calculations of the static pressure on the side opposite of the absolute pressure transducer by $p_1 = p_2 - \Delta p$ significantly alter the signal for higher frequencies or amplitudes and thus have high uncertainties.

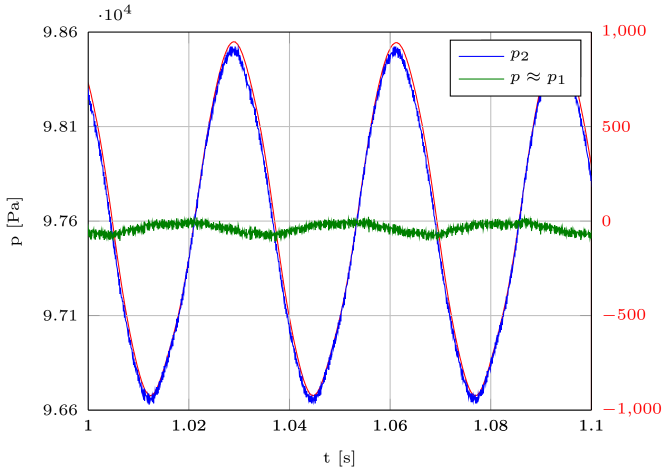

Figure 5.23.: Comparison of absolute pressure transducer signal and signal of differential pressure transducer, which was converted to a relative pressure transducer, at 31 Hz and low amplitude. p_1 approximated by $(p_2 - \Delta p)$.

Steady Flow Calibration

During the steady flow calibration measurements, oscillations at a frequency around 140 Hz with amplitudes up to 25 % of the mean differential pressure were present in the pressure signals. A similar behavior has already been reported by Doblhoff-Dier [34] for the same device at slightly higher frequencies. There, a combination of resonances in the main pipe and in the pressure measurement system was suspected and made responsible for the occurring pulsations.

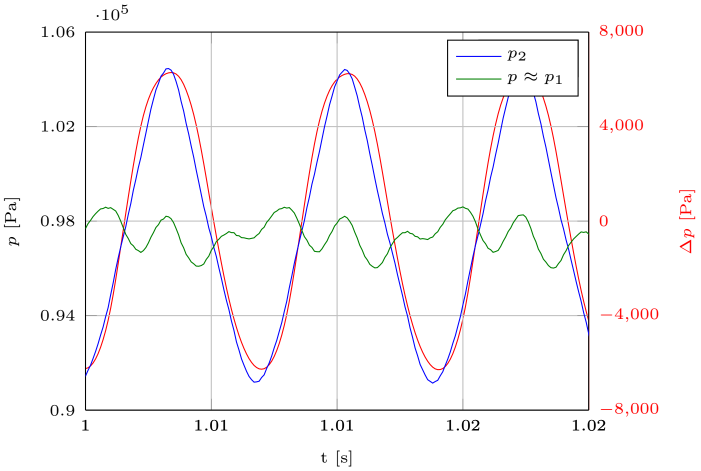

Figure 5.24.: Comparison of absolute pressure transducer signal and signal of differential pressure transducer, which was converted to a relative pressure transducer, at 142 Hz and high amplitude. p_1 approximated by $(p_2 - \Delta p)$.

As is discussed below, the spectral peak at the frequency in question is clearly identified as a resonance frequency of the pressure measurement system, justifying the theory about the coupling between resonance pipe and connecting tubes. The lower resonance frequency in this work compared to Doblhoff-Dier can be explained by the additional volumes connected to the pressure measurement system for the static pressure transducer and the volume compensation tube on the opposite side. The resonance frequency itself, is well below what can be anticipated from $\lambda/4$-waves in the pressure gauge lines, but a Helmholtz resonance behavior including the volume of the connecting ports around the orifice as discussed in section 2.6.2 could explain the low frequencies.

Another investigated explanation for the occurring oscillations, was the shedding of vortices at the orifice plate due to weak resonance pulsations in the main pipe, creating additional fluctuations in pressure at the downstream tapping. According to Sigurdson et al. [52], vortices at the edge of an orifice would be shed at the frequency of an inducing pulsation, narrowing the downstream jet periodically. This results in a periodic increase/decrease of the Venturi effect and an oscillating downstream pressure can be measured, due to the varying Bernoulli effect. The fact, that the pulsations at steady flow could be detected with the static pressure transducer at the upstream tapping to an equal extent, indicated that vortex shedding, although most certainly occurring, is not the root of the high differential pressure oscillations measured.

If the pulsations can be attributed to resonances in the connecting tubes, the resulting pressure at the transducers will be a superposition of the approximately constant, steady pressures at the tappings and the standing waves in the connecting tubes. In the case of a symmetric deflections, the time average of the pressure signal then provides the correct pressure at the tappings. Applying a digital low-pass filter to cut off frequencies equal to and above the resonance frequency for all later measurements, in the same manner as it was done by Doblhoff-Dier, was deemed unsuitable for accurate unsteady flow measurement. The reason being that the spectral analysis of the simulated sinusoidal pulsations at significantly lower frequencies revealed differential pressure responses in the frequency range of question (see Fig. 5.9).
Figure 5.4 shows the one second time averaged kinematic pressure differences measured in both directions, where the direction of flow is indicated by the upstream (US) or downstream (DS) position of the absolute pressure transducer. The time averaged flow rate measurements showed good agreement with the steady CFD simulations in the measurement range and no significant difference in the pressure difference for reverse flow could be detected. However, the low permissible flow rate severely limits the conclusions that can be drawn from the calibration measurements.
Since higher pressure differences were encountered in later measurements, flow rates above 600 l/min have been extrapolated with a quadratic regression of the measurements up to 600 l/min.

In light of the above discussion about the pressure oscillations in steady flow, the recommendation to shorten pressure gauge lines has to be stressed for future work. It was not done in this work, since initially measurements at exhaust flows were planned and short connection tubes would pose the risk of damaging the pressure transducers in hot exhaust gas. A change in the layout of the device and a significant reduction of the connection tube lengths, however, is essential in order reduce measurement errors or to further restrict error sources to the pressure transducers or unconsidered flow effects at the orifice.

Resonance Modes

Plotted in figure 5.25 are the power spectral densities of the pressure signals acquired with the orifice in the main pipe while white noise was applied to the acoustic driver. The resonance peaks are clearly visible therein and compare well to the numerically calculated, anticipated resonance modes for a setup without orifice 5.26, although calculated frequencies generally were about 4 Hz too high. Only considering frequencies up to 200 Hz, resonance modes could be located with this method at 29, 56, 83, 111, 139, 166, and 194 ± 1 Hz, which correspond to $n \cdot \lambda/4$ - waves with $n = 3, 5, 7, ..., 15$. In the course of the subsequent measurements, resonance frequencies varied about ± 1 Hz, because of small variations in pipe length for each specific setup.

Spectral densities of the measured response showed a rise in magnitude at frequencies around 140 Hz, which again is mainly attributed to the resonance of the pressure measurement system. Nonetheless frequency dependent sensitivity of the loudspeaker (i.e. output sound pressure level) and damping characteristics of the resonance pipe setup are most definitely contributing to the shape of the response spectra. Due to the constant spectral power of a white noise signal and the sensitivity of the driver, the lowest resonance mode ($L = \lambda/4$) at 7 Hz for example, could not be detected in the response. Since the exact impact of above listed effects was of low importance to the subsequent single component excitation experiments, no further investigations were carried out on this subject.

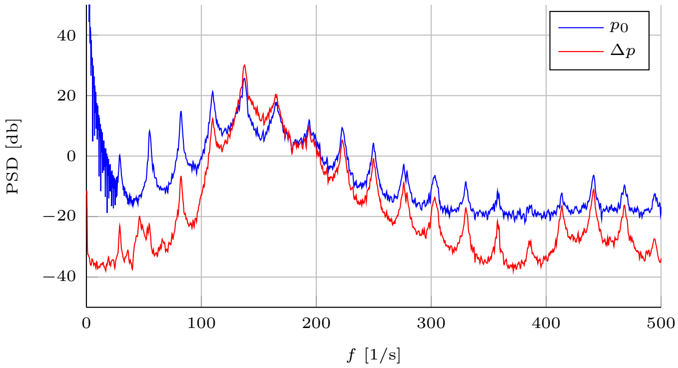

Figure 5.25.: Power spectral densities of measured absolute and differential pressures in resonance pipe during excitation with white noise, calculated with Welch's method.

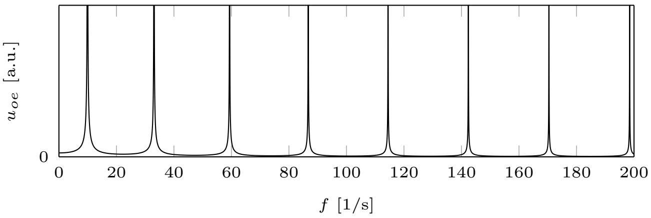

Figure 5.26.: Numerically calculated frequency response of particle velocity at open end (u_{oe}) to sinusoidal excitations of acoustic driver.

5.3.2. Resonance Frequency Excitation

Drawn in figure 5.27 is an example of the measured pressure signals at the first antinode (counted from open end) for an excitation with the speaker at 139 Hz. Although zero differential pressure was expected there, a response in the order of magnitude of the static pressure could be measured for all driver output levels. Differential pressures in the order of $5 \cdot 10^3$ Pa would correspond to oscillations between -30 and 30 m/s mean flow velocity, which is highly unlikely for the given setup. Additionally, the pressure difference showed an asymmetric behavior with respect to zero, which continuously increased with increasing driver power. In the case of the measurements depicted in Fig. 5.27, this asymmetry resulted in a mean differential pressure of $-100Pa$. An offset of this magnitude translates to significant flow rates, which can not be explained by a process creating mean flow and a leakage in the setup. The same anomalies could be found at the second pressure antinode.

Both phenomena though can be explained by the presence of the before mentioned resonances in the pressure measurement system. When the standing wave in the main pipe is inducing resonances in the connecting tubes of the pressure measurement system, differences in amplitude, frequency and/or phase of the resonances in the two sides of the pressure measurement system, then would lead to an asymmetric measured differential pressure.

All ensuing measurements were significantly influenced by the resonance magnification of the pressure measurement system, since higher order harmonics of the resonance modes below 80 Hz in the main pipe were drastically increased by the resonance. Nevertheless it was attempted to make an assessment of the proposed procedure to determine the unsteady friction parameter at 30 Hz. At this frequency resonances were present, but of minor extent compared to higher resonance modes.

Figures 5.28 and 5.29 show the measured pressure signals at the pressure antinode and node, respectively. The pressure signal spectral components at 30 Hz are given table 5.3. At the antinode a pressure maximum of 3200 ± 100 Pa was

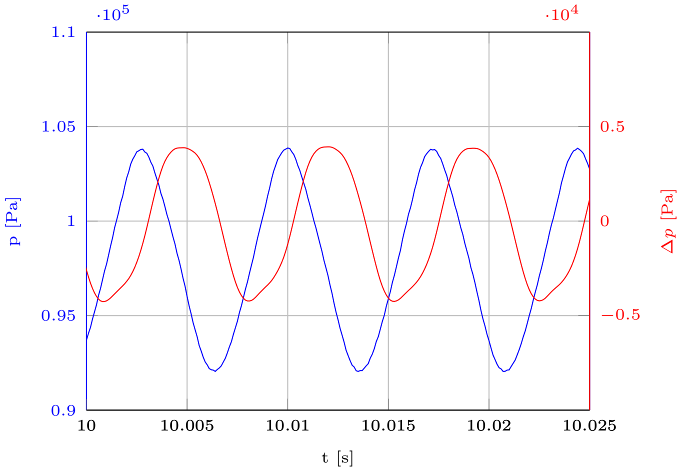

Figure 5.27.: Measured absolute and differential pressure at 139 Hz with orifice located at pressure antinode.

found, but the measured differential pressure could not be reduced any further by varying the position of the orifice plate. At the node, the superimposed resonances of the pressure measurement system (146 Hz) are clearly visible.

Table 5.3.: Fourier components of absolute and differential pressure signals at 30 Hz with orifice located at pressure antinode and node.

location	p_2 [Pa]	Δp [Pa]
antinode	3200 ± 100	15 ± 10
node $-0.38\ m$	480 ± 50	190 ± 10

Using the pressure amplitude of $p = 3200 \pm 100\ Pa$ at the antinode, measured quiescent density $\rho_0 = 1.165 \pm 0.005\ kg/m^3$ and static pressure $p_0 = 97810 \pm 20\ Pa$, allows to estimate the amplitude of the standing wave velocity to $U = 8.0 \pm 0.3\ m/s$. Also considering the positional displacement of 0.38 m of the

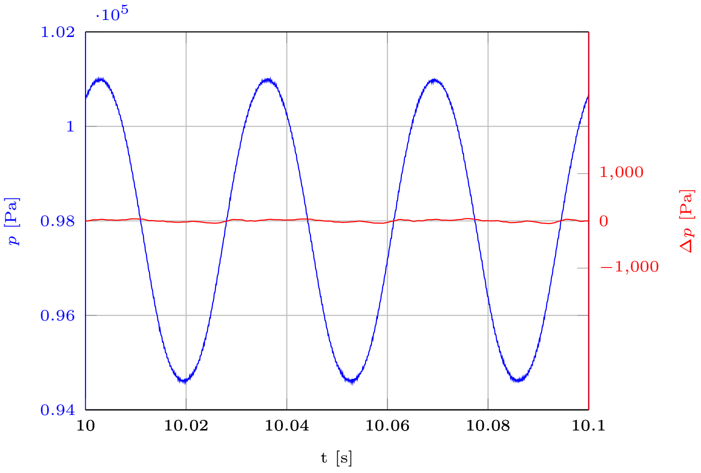

Figure 5.28.: Measured absolute and differential pressure at 30 Hz with orifice located at pressure antinode.

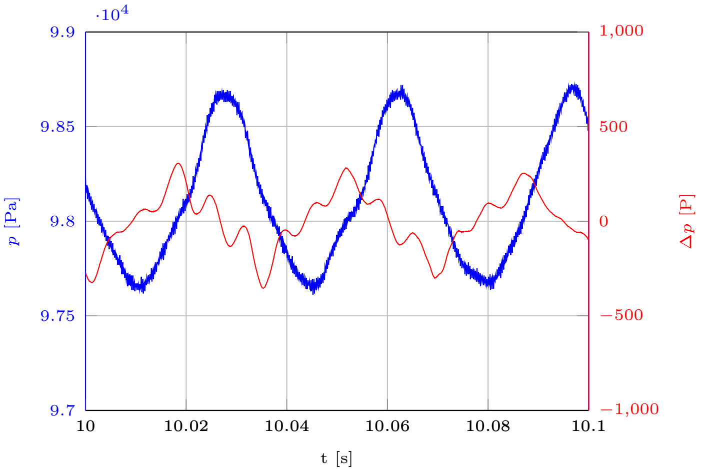

Figure 5.29.: Measured absolute and differential pressure at 30 Hz with orifice located at a distance of 0.38 m from pressure node.

measurement location from the actual node location at 30 Hz, would reduce the amplitude of the standing wave velocity to $U = 7.8 \pm 0.3\ m/s$. This calculation, however, does not account for viscous losses in the pipe and at the orifice, which would further reduce the velocity amplitude. Although, previous research has shown, that orifice resistances are close to zero, when mean flow is zero [53]. The calculated velocity amplitude is in agreement with the calculations of the flow velocity with the unsteady friction model ($k = 5.4$), plotted in figure 5.31.

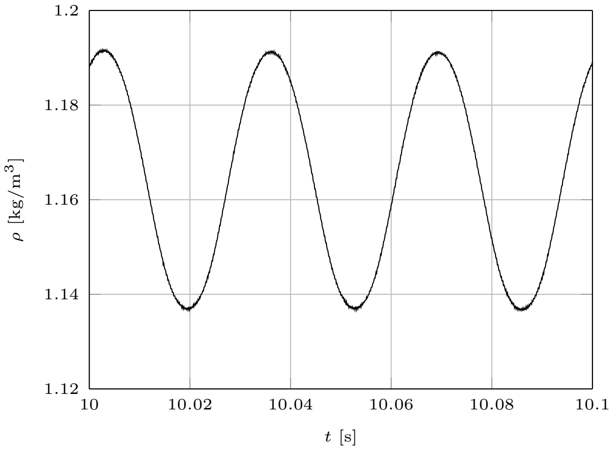

Figure 5.30.: Calculated density for 30 Hz measurement, with the orifice located at pressure antinode.

At this point we have to refrain from a further interpretation of the above result and from trying to determine the actual calibration parameter k for two reasons. Primarily, measurement errors introduced by the resonances in the pressure measurement system and the uncertainties that come with a simple spectral analysis of a distorted signal are too large to allow an exact calculation. Secondly, all considerations above neglected the influence that the orifice plate poses to the standing waves inside the main duct. Moving the orifice meter for the measurement of both, the pressure node and antinode, most certainly introduces a significant error, because the pulsation amplitude inside the duct will likely change with the repositioning of the orifice. Additionally, as was mentioned before and could be seen from the simulations at 30 Hz, inertial effects at frequencies this low are still subordinate, making an accurate determination inherently difficult.

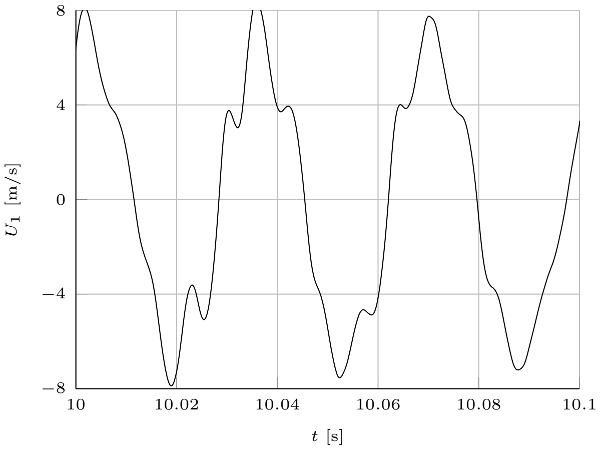

Figure 5.31.: Calculated flow velocity for 30 Hz measurement, with the orifice located at a distance of 0.38 m from pressure node. An unsteady friction parameter of $k = 5.4$ was used.

5.3.3. Proposed Setup Modifications

To overcome the shortcomings of the setup used in this work, two suggestions for a modified setup for future work will be listed below.

- Most importantly the layout of the the orifice meter has to be changed. The tubes connecting the pressure transducers to the orifice have to be shortened, to eliminate one error source of resonances in the pressure measurement system. If resonances are persistent, the pressure transducers should be re-evaluated.

- To be able to simultaneously measure orifice differential pressure, i.e. mass flow, at a pressure node and measure standing wave amplitudes at an antinode, an additional pressure transducer should be installed between orifice meter and driver. It would be useful to add a second transducer at a pressure antinode between orifice and open end, to have the ability to measure a possible attenuation or phase shift of the pressure on the open end side of the orifice. This of course would only be possible from the $5 \cdot \lambda/4$

resonance mode upwards (56 Hz in our case).

6. Conclusions

In an effort to improve and advance time-resolved engine intake and exhaust gas flow measurement utilizing orifice meters without pulsation dampers, an attempt was made to verify the relation between measured pressure difference and mass flow rate at an orifice and enhance measurements by accounting for fast density changes that are present in exhaust flows.

A review of literature and theoretical considerations about the flow of fluids in steady and pulsating flows highlighted deviations in the flow fields in the vicinity of the orifice from the flow fields presumed for conventional temporal inertia theory orifice mass flow equations.

No proper incorporation of the increase in pressure difference due to the stagnation the orifice plate in a corner tapping configuration could be found for steady orifice flow theory. This was extensively discussed, since CFD simulations of steady flow at a variety of flow speeds showed, that approximately half of the differential pressure measured at an orifice in a corner tapping configuration is a result of the stagnation at the upstream side of the orifice plate. The big influence of this impact pressure on the measured pressure differential, seems to invalidate the simple Bernoulli equation approach of explaining the pressure differences measured in steady flows with the duct to vena contracta area ratio. Although this is of little importance in steady flow measurement, because only the total functional relation between pressure difference and mass flow is needed for calibration, an incomplete consideration of this flow phenomenon inevitably leads to metering errors and interpretation deficiencies in unsteady flow measurement.

Following the encountered, well documented discrepancy between the quasi-steady flow assumption that underlies inertial theory and the flow occurring at orifices in pulsating flows, paired with the concerns of previous research by AVL List GmbH, that the influence of the uncertainties of discharge coefficients and temporal inertia may not allow for an accurate measurement with the use of orifices, an alternative unsteady mass flow equation in a control region approach was proposed. The use of an unsteady friction model, which accounts for unsteady pressure losses in dependence of the local acceleration, backs up the fundamental relation between temporal change of mass flow and measured pressure difference in the temporal inertia theory. It additionally could explain the high losses previously observed in unsteady orifice flow. The found increase of effective inertia through friction would eliminate the need of an effective length that proves elusive to define in terms of fluid dynamics. However, as was shown with the use of transient CFD simulations, assuming a constant unsteady friction parameter or constant inertia clearly introduces high errors to the predicted mass flow of pulsatile flows when considerable deviations from a quasi-steady flow field are present, e.g. when local flow reversal occurs. It may be possible to correctly capture this behavior by allowing a variability of the unsteady friction in dependence of the local acceleration or by additionally allowing a dependence on the convectional acceleration, but this unavoidably would introduce an additional constant in need of calibration. A constructional way of reducing the unsteady flow effects could be to decrease the orifice hole diameter by using a multi-hole orifice and thereby force the flow to a quasi-steady behavior. Admittedly, this needs to be validated first by more CFD simulations.

The low errors achieved in the simulations for situations when the pulsation amplitude is smaller than the bias flow validate the approach for pulsating intake and exhaust flow measurement, if an accurate determination of the unsteady friction parameter is experimentally possible and differential pressures can be acquired correctly. Because of the high errors introduced by a wrong unsteady friction parameter or inertial coefficient due to inertial and square root errors, a precise determination of the unsteady friction parameter remains the main priority for improving unsteady measurements. For the same reason, taking into account the temporal density changes in the model should be considered of secondary importance. Nevertheless, the need of fast and accurate gas density determination can be addressed by the presented method of combining the two thermocouple compensation method with an adiabatic correction of the measured temperature.

The experimental approach of determining the calibration parameters in a standing wave resonance pipe was shown to be heavily influenced by the presence of resonances in the pressure measurement system. It is crucial for future work with the device to determine the exact root of the resonances, before any further measurements can be conducted. An adverse interference due to the overlap in the measured pressure signal of frequency components that are flow induced and resonance frequencies of the pressure measurement system certainly has to be expected. If the assumption, that the unwanted resonances stem from a Helmholtz resonance behavior is correct, shortening the connection tubes would immediately shift the resonance frequencies upwards. Any offset in the measured pressure difference signal that is not mean flow induced should be removed thereby.
Regarding the calibration principle itself, results at 30 Hz did show the essential feasibility of the approach, but for a precise determination of the calibration parameters, an improvement of the setup by including additional pressure transducers is necessary, to allow for a better characterization of the pulsations inside the resonance tube.

Appendix

Appendix A.

OpenFOAM dictionaries

A.1. fvSchemes

```
/*--------------------------------*- C++ -*----------------------------------*\
| =========                 |                                                 |
| \\      /  F ield         | OpenFOAM: The Open Source CFD Toolbox           |
|  \\    /   O peration     | Version:  2.3.0                                 |
|   \\  /    A nd           | Web:      www.OpenFOAM.org                      |
|    \\/     M anipulation  |                                                 |
\*---------------------------------------------------------------------------*/
FoamFile
{
    version     2.0;
    format      ascii;
    class       dictionary;
    location    ”system”;
    object      fvSchemes;
}
// * * * * * * * * * * * * * * * * * * * * * * * * * * * * * * * * * * * * * //

ddtSchemes
{
    default         Euler;
}

gradSchemes
{
    default         leastSquares;
}

divSchemes
{
    default         none;
    div(phi,U)      Gauss upwind;
    div(phid,p)     Gauss upwind;
    div(phi,K)      Gauss linear;
    div(phi,h)      Gauss upwind;
    div(phi,k)      Gauss upwind;
    div(phi,epsilon) Gauss upwind;
```

```
    div(phi,R)        Gauss upwind;
    div(phi,omega)    Gauss upwind;
    div((rho*R))      Gauss linear;
    div(R)            Gauss linear;
    div(U)            Gauss linear;
    div((muEff*dev2(T(grad(U))))) Gauss linear;
}

laplacianSchemes
{
    default           Gauss linear corrected;
}

interpolationSchemes
{
    default           linear;
}

snGradSchemes
{
    default           corrected;
}

fluxRequired
{
    default           no;
    p                 ;
}
// ************************************************************************* //
```

A.2. fvSolution

```
/*--------------------------------*- C++ -*----------------------------------*\
| =========                 |                                                 |
| \\      /  F ield         | OpenFOAM: The Open Source CFD Toolbox           |
|  \\    /   O peration     | Version:  2.3.0                                 |
|   \\  /    A nd           | Web:      www.OpenFOAM.org                      |
|    \\/     M anipulation  |                                                 |
\*---------------------------------------------------------------------------*/
FoamFile
{
    version     2.0;
    format      ascii;
    class       dictionary;
    location    "system";
    object      fvSolution;
}
// * * * * * * * * * * * * * * * * * * * * * * * * * * * * * * * * * * * * * //

solvers
{
    p
    {
        solver          PCG;
        preconditioner  DIC;
        tolerance       1e-08;
        relTol          0.01;
    }
```

```
    pFinal
    {
        $p;
        tolerance       1e-08;
        relTol          0;
    }

    ”(rho|U|h|k|epsilon|omega)”
    {
        solver          smoothSolver;
        smoother        symGaussSeidel;
        tolerance       1e-07;
        relTol          0.1;
    }

    ”(rho|U|h|k|epsilon|omega)Final”
    {
        $U;
        tolerance       1e-07;
        relTol          0;
    }

}

PIMPLE
{
    momentumPredictor yes;
    transonic       no;
    nOuterCorrectors 3;
    nCorrectors     4;
    nNonOrthogonalCorrectors 5;
    rhoMin          rhoMin [ 1 -3 0 0 0 ] 0.5;
    rhoMax          rhoMax [ 1 -3 0 0 0 ] 2;

    residualControl
    {
        ”(U|k|epsilon)”
        {
            relTol          0;
            tolerance       0.0001;
        }
    }

    turbOnFinalIterOnly off;
}

relaxationFactors
{
    fields
    {
        ”p.*”           0.3;
        ”rho.*”         0.1;
    }
    equations
    {
        ”(U|h|k|epsilon|omega).*” 0.7;
    }
}
// ************************************************************************* //
```

Bibliography

[1] RC Mottram. “The behaviour of orifice and Venturi-nozzle meters in pulsating flow.” PhD thesis. University of Surrey, 1971 (cit. on pp. v, 22, 25, 49).

[2] ISO/TR 3313: 1998. *Measurement of the Flow of a Fluid Medium in Closed Channels. Manual on the Effect of Fluctuations of a Flow on Flow Rate Measurement Devices.* Tech. rep. (cit. on pp. vi, 63).

[3] Willard W Pulkrabek. *Engineering fundamentals of the internal combustion engine.* Vol. 478. Prentice Hall Upper Saddle River, NJ, 1997 (cit. on pp. 3, 4, 31, 36).

[4] Michael Wiesinger. “Entwicklung eines Abgas-Massenflußsensors.” PhD thesis. Technische Universität Wien, 1999 (cit. on p. 3).

[5] Richard Van Basshuysen and Fred Schäfer. *Handbuch Verbrennungsmotor: Grundlagen, Komponenten, Systeme, Perspektiven.* Springer-Verlag, 2010 (cit. on p. 4).

[6] Ronald L Panton. *Incompressible flow.* John Wiley & Sons, 2006 (cit. on pp. 4, 6, 8).

[7] Erich Truckenbrodt. *Fluidmechanik: Bd. 1: Grundlagen und elementare Strömungsvorgänge dichtbeständiger Fluide.* Springer Verlag, 1980 (cit. on pp. 4, 6, 9, 10).

[8] Mohamed S Ghidaoui et al. “A review of water hammer theory and practice.” In: *Applied Mechanics Reviews* 58.1 (2005), pp. 49–76 (cit. on pp. 6, 14).

[9] RA Bajura and MT Pellegrin. “Studies of pulsating incompressible flow through orifice meters.” In: *Symposium on Flow in Open Channel and Closed Conduits.* NDS. 1977 (cit. on p. 11).

[10] Alexander Yakhot, Leopold Grinberg, and Nikolay Nikitin. “Simulating pulsatile flows through a pipe orifice by an immersed-boundary method.” In: *Journal of fluids engineering* 126.6 (2004), pp. 911–918 (cit. on p. 11).

[11] EG Richardson and E Tyler. “The transverse velocity gradient near the mouths of pipes in which an alternating or continuous flow of air is established.” In: *Proceedings of the Physical Society* 42.1 (1929), p. 1 (cit. on p. 11).

[12] Theodor Sexl. “Über den von EG Richardson entdeckten Annulareffekt.” In: *Zeitschrift fuer Physik* 61.5-6 (1930), pp. 349–362 (cit. on p. 11).

[13] Shigeo Uchida. “The pulsating viscous flow superposed on the steady laminar motion of incompressible fluid in a circular pipe.” In: *Zeitschrift fuer angewandte Mathematik und Physik ZAMP* 7.5 (1956), pp. 403–422 (cit. on pp. 11, 12).

[14] A Yakhot, M Arad, and G Ben-Dor. “Numerical investigation of a laminar pulsating flow in a rectangular duct.” In: *International journal for numerical methods in fluids* 29.8 (1999), pp. 935–950 (cit. on pp. 11, 12).

[15] S He and JD Jackson. “An experimental study of pulsating turbulent flow in a pipe.” In: *European Journal of Mechanics-B/Fluids* 28.2 (2009), pp. 309–320 (cit. on p. 11).

[16] JW Daily et al. *Resistance coefficients for accelerated and decelerated flows through smooth tubes and orifices.* Tech. rep. DTIC Document, 1955 (cit. on pp. 14, 23).

[17] B Brunone, UM Golia, and M Greco. “Some remarks on the momentum equation for fast transients.” In: *Proc. Int. Conf. on Hydr. Transients With Water Column Separation.* 1991, pp. 201–209 (cit. on p. 14).

[18] Anton Bergant, Angus Ross Simpson, and John Vitkovsk. “Developments in unsteady pipe flow friction modeling.” In: *Journal of Hydraulic Research* 39.3 (2001), pp. 249–257 (cit. on p. 14).

[19] DIN EN ISO 5167-1:2004-01. *Measurement of fluid flow by means of pressure differential devices inserted in circular cross-section conduits running full - Part 1: General principles and requirements (ISO 5167-1:2003).* Tech. rep. (cit. on pp. 19, 21).

[20] DIN EN ISO 5167-2:2004-01. *Measurement of fluid flow by means of pressure differential devices inserted in circular cross-section conduits running full - Part 2: Orifice plates (ISO 5167-2:2003).* Tech. rep. (cit. on p. 19).

[21] MJ Reader-Harris and JA Sattary. “The orifice plate discharge coefficient equation.” In: *Flow Measurement and Instrumentation* 1.2 (1990), pp. 67–76 (cit. on p. 20).

[22] PM Downing. “Effect of Pulsating Flow Upon Metering By Square Edged Orifices.” PhD thesis. University of Surrey, 1975 (cit. on p. 22).

[23] V.G. Szebehely. “A Measure of the Unsteadiness of Time-Dependent Flows.” In: *Proc. Third Midwestern Conference on Fluid Mechanics* (1953) (cit. on p. 22).

[24] A.K. Oppenheim and E.G. Chilton. “Pulsating Flow Measurements - A Literature Survey.” In: *Trans. ASME* (1955) (cit. on p. 22).

[25] Rudolf Krüger. *Strömungserscheinungen an einer Blende in oszillierender Rohrströmung.* Technische Universitaet. Institut fuer Wasserbau und Wasserwirtschaft, 1977 (cit. on p. 23).

[26] Andreas Schlenkhoff. “Druckverluste an Blenden in einer oszillierenden Rohrstroemung.” PhD thesis. Bergische Univ.-Gesamthochsch., Lehr-und Forschungsgebiet Wasserbau und Wasserwirtschaft, 1991 (cit. on p. 23).

[27] R McKee. “Pulsation Effects on Orifice Metering Considering Primary and Secondary Elements.” In: *Proc. Proceedings of the 22nd Gulf Coast Measurements Short Course* (1989), pp. 112–118 (cit. on pp. 23, 24).

[28] WA Mohammad and RC Mottram. “High frequency pulsation effects on orifice meter accuracy.” In: *Proc. Int. Conf. on Advances in Flow Measurement Techniques*. University of Warwick, BHRA Fluid Engineering. 1981 (cit. on p. 23).

[29] Katharina Doblhoff-Dier et al. “Time resolved measurement of pulsating flow using orifices.” In: *Flow Measurement and Instrumentation* 22.2 (2011), pp. 97–103 (cit. on p. 25).

[30] P Hebrard et al. “An investigation of the behaviour of orifice meter in pulsating flow conditions.” In: *FLOMEKO 85, Melbourne*. 1985 (cit. on p. 25).

[31] Andreas Brümmer, Patrick Tetenborg, and Roland Edlerherr. *Numerische und experimentelle Untersuchung pulsierender Strömungen in Wirkdruckmesseinrichtungen am Beispiel einer Blende*. Tech. rep. Technische Universität Dortmund, 2014. URL: `http://www.koetter-consulting.com/coRED/_data/07_TU_Dortmund_Tetenborg.pdf` (cit. on p. 25).

[32] Lawrence E Kinsler et al. “Fundamentals of acoustics.” In: *Fundamentals of Acoustics, 4th Edition, by Lawrence E. Kinsler, Austin R. Frey, Alan B. Coppens, James V. Sanders, pp. 560. ISBN 0-471-84789-5. Wiley-VCH, December 1999.* 1 (1999) (cit. on pp. 26–29).

[33] Ivan Bajsić, Jože Kutin, and Tomaž Žagar. “Response time of a pressure measurement system with a connecting tube.” In: *Instrumentation Science and Technology* 35.4 (2007), pp. 399–409 (cit. on p. 29).

[34] K Doblhoff-Dier. “Assessment of Technological Approaches for Exhaust Mass Flow Measurement Using Differential Pressure Devices.” MA thesis. Vienna University of Technology, 2010 (cit. on pp. 29, 31, 62, 63, 68, 94).

[35] P.C. Hung et al. “Difference equation approach to two-thermocouple sensor characterization in constant velocity flow environments.” In: *Review of Scientific Instruments* 76.2 (Feb. 2005), pages. ISSN: 0034-6748. DOI: `10.1063/1.1847412` (cit. on pp. 32, 34).

[36] Kar K.; Roberts S.; Stone R.; Oldfield M. et al. "Instantaneous Exhaust Temperature Measurements Using Thermocouple Compensation Techniques." In: *SAE International* (2004). 2004-01-1418. DOI: `doi:10.4271/2004-01-1418` (cit. on p. 32).

[37] Scadron Marvin D.; Warshasky Isidor. *Experimental determination of time constants and Nusselt numbers for bare-wire thermocouples in high-velocity air streams and analytic approximation of conduction and radiation errors.* Tech. rep. NACA, 1952. URL: `http://wayback.archive-it.org/1792/20100130051500/http://hdl.handle.net/2060/19930083429` (cit. on p. 32).

[38] M Tagawa and Y Ohta. "Two-thermocouple probe for fluctuating temperature measurement in combustion—Rational estimation of mean and fluctuating time constants." In: *Combustion and flame* 109.4 (1997), pp. 549–560 (cit. on p. 34).

[39] Hans Pfriem. "Zur Messung veränderlicher Temperaturen von Gasen und Flüssigkeiten." German. In: *Forschung auf dem Gebiet des Ingenieurwesens A* 7.2 (1936), pp. 85–92. ISSN: 0015-7899. DOI: `10.1007/BF02592988`. URL: `http://dx.doi.org/10.1007/BF02592988` (cit. on p. 34).

[40] Seán McLoone et al. "Exploiting a priori time constant ratio information in difference equation two-thermocouple sensor characterization." In: *Sensors Journal, IEEE* 6.6 (2006), pp. 1627–1637 (cit. on p. 34).

[41] CS Burrus and TW Parks. "Digital filter design." In: *New York* (1987) (cit. on p. 35).

[42] Jung Seob Kim and Navneet Radheshyam Singh. "A Novel Adiabatic Pipe Flow Equation for Ideal Gases." In: *Journal of Fluids Engineering* 134.1 (2012), p. 011202 (cit. on p. 36).

[43] (Cit. on p. 41).

[44] Jagannath Rajasekaran. "On the flow characteristics behind a backward-facing step and the design of a new axisymmetric model for their study." PhD thesis. University of Toronto, 2011 (cit. on p. 48).

[45] (Cit. on p. 53).

[46] Christophe Geuzaine and Jean-François Remacle. "Gmsh: A 3-D finite element mesh generator with built-in pre-and post-processing facilities." In: *International Journal for Numerical Methods in Engineering* 79.11 (2009), pp. 1309–1331. URL: `http://geuz.org/gmsh/` (cit. on p. 53).

[47] *OpenFOAM - The Open Source CFD Toolbox, User Guide* (cit. on p. 55).

[48] User's Guide Fluent. "Fluent 6.1." In: *New Hampshire Company, Fluent Incorporation, Lebanon, USA* (2001) (cit. on p. 55).

[49] *Product Guide, AVL 442 BLOW BY METER* (cit. on p. 66).

[50] David Marx, Xiaoan Mao, and Artur J Jaworski. "Acoustic coupling between the loudspeaker and the resonator in a standing-wave thermoacoustic device." In: *Applied Acoustics* 67.5 (2006), pp. 402–419 (cit. on p. 70).

[51] Pavel Holoborodko. *Smooth Noise Robust Differentiators.* http://www.holoborodko.com/pavel/methods/numerical-derivative/smooth-low-noise-differentiators/. 2008 (cit. on p. 72).

[52] Lorenz W Sigurdson and D Chapple. "A turbulent mechanism for pulsation-induced orifice plate flow meter error." In: *Proceedings of the 13th Australasian Fluid Mechanics Conference, Eds. Thompson MC and Hourigan K, Monash U, Australia.* Vol. 1. 1998, pp. 13–18 (cit. on p. 95).

[53] Hans Boden and Lin Zhou. "Acoustic properties of an in-duct orifice subjected to bias flow and high level acoustic excitation." In: *10th International Conference on Flow-Induced Vibration (& Flow-Induced Noise); Dublin, Ireland, 2nd-6th July 2012.* 2012, pp. 187–193 (cit. on p. 102).